

1 **2021-07-11789 Revised**

2 **Immune, endothelial and neuronal network map in human lymph node and spleen**

3

4 Seth Currlin<sup>1,2</sup>, Harry S. Nick<sup>1</sup>, Marda Jorgensen<sup>3</sup>, Jerelyn A. Nick<sup>3</sup>, Maigan A. Brusko<sup>3</sup>, Hunter  
5 Hakimian<sup>2</sup>, Jesus Penalosa-Aponte<sup>3</sup>, Natalie Rodriguez<sup>3</sup>, Miguel Medina-Serpas<sup>3</sup>, Mingder  
6 Yang<sup>3</sup>, Robert P. Seifert<sup>3</sup>, Irina Kusmartseva<sup>3</sup>, Todd M. Brusko<sup>3,4</sup>, Kevin Otto<sup>2</sup>, Amanda L.  
7 Posgai<sup>3</sup>, Clive H. Wasserfall<sup>3</sup>, Mark A. Atkinson<sup>3,4\*</sup>

8

9 <sup>1</sup>Department of Neuroscience, College of Medicine, University of Florida, 1149 Newell Drive,  
10 Room L1-100, Gainesville, FL 32601.

11 <sup>2</sup>J. Crayton Pruitt Family Department of Biomedical Engineering, Herbert Wertheim College of  
12 Engineering, University of Florida, 1275 Center Drive, Biomedical Sciences Building, 3<sup>rd</sup> Floor,  
13 Gainesville, FL 32611.

14 <sup>3</sup>Department of Pathology, Immunology, and Laboratory Medicine, Diabetes Institute, College of  
15 Medicine, University of Florida, 1275 Center Drive, Biomedical Sciences Building, 5<sup>th</sup> Floor,  
16 Gainesville, FL 32611.

17 <sup>4</sup>Department of Pediatrics, College of Medicine, University of Florida, 1600 SW Archer Road,  
18 Gainesville, FL 32610.

19

20 Words: 2,730

21 Display items: 5 Figures

22 References: 78

23 Methods References: 3

24 Extended Data: 11 Figures, 1 Table

25 Supplementary Information: 1 Table, 6 Videos

26 **Summary**

27 The spleen and lymph node represent important hubs for both innate and adaptive immunity<sup>1,2</sup>.  
28 Herein, we map immune, endothelial, and neuronal cell networks within these tissues from  
29 “normal”/non-diseased organ donors, collected through the NIH Human BioMolecular Atlas  
30 Program (HuBMAP)<sup>3</sup>, using highly multiplexed CODEX (CO-Detection by indEXing) imaging  
31 and 3D light sheet microscopy of cleared tissues. Building on prior reports<sup>4-6</sup>, we observed the  
32 lymph node subcapsular sinus expressing podoplanin, smooth muscle actin, and LYVE1. In the  
33 spleen, LYVE1 was expressed by littoral cells lining venous sinusoids, whereas podoplanin was  
34 restricted to arteries and trabeculae. 3D visualization of perivascular innervation revealed a  
35 subset of axonal processes expressing choline acetyl transferase in both tissues, in contrast  
36 with prior literature on human spleen<sup>7</sup>. We further report our novel observations regarding the  
37 distinct localization of GAP43 and  $\beta$ 3-tubulin within the vascular anatomy of both lymph node  
38 and spleen, with Coronin-1A+ cells forming a dense cluster around  $\beta$ 3-tubulin positive GAP43  
39 low/negative segments of large vessels in spleen. These data provide an unprecedented 2D  
40 and 3D visualization of cellular networks within secondary lymphoid tissues, laying the  
41 groundwork for future disease-specific and system-wide studies of neural regulation of immunity  
42 in human lymphatics.

43 **Main**

44 With similarities to the circulation, the lymphatic system stretches across the entire human  
45 body<sup>8,9</sup> to provide the critical functions of conducting lymphatic fluid, filtering blood, mounting  
46 defenses against infections and cancer, and shaping immune cell responses to protect against  
47 pathogens and autoimmune diseases<sup>8,9</sup>. Tissue organization and function are directly linked in  
48 spleen (SPL; blood filtration) and lymph nodes (LN; interstitial fluid filtration) facilitating immune  
49 cell priming and activation within follicles as well as afferent and efferent migration through  
50 vessels, ducts, and sinusoids<sup>9</sup>. The autonomic nervous system provides control of host immune  
51 defense mechanisms through innervation from sympathetic postganglionic neurons, specifically  
52 the splenic nerve for the SPL and anatomically paired nerve fibers for respective LNs<sup>10</sup>.  
53 However, much of our knowledge regarding the architecture and function of the lymphatic  
54 system derives from rodents<sup>11</sup>, with recent studies noting a series of key architectural  
55 differences compared to humans<sup>12-14</sup>.

56 Indeed, recent 3D imaging and topological mapping of the murine LN<sup>15,16</sup> have described  
57 a mesh-like network composed of fibroblastic reticular cells (FRCs) that provide the homing  
58 zone for T cells and may mediate B cell homeostasis<sup>17</sup>. Moreover, Huang and colleagues  
59 recently demonstrated the murine LN capsule to be encased by a network of sensory neurons  
60 capable of neuroimmune transcriptional regulation<sup>18</sup>. The delivery of antigens<sup>19</sup>, inflammatory  
61 mediators, and even larger molecules<sup>20</sup> to the LN T cell zone involves the transport of lymph  
62 initially filtered through the subcapsular sinus, followed by passage along an elaborate  
63 lymphatic conduit system<sup>21</sup>. Similarly, Ogembo et al.<sup>13</sup> and Buckley et al.<sup>22</sup> have elegantly  
64 described SIRP $\alpha$ , FHOD1, HLA-DR, CD36 (platelet glycoprotein IV), CD71 (transferrin receptor)  
65 and CD8 $\alpha$  as cell markers expressed by littoral cells (LCs) lining the splenic sinusoids. LCs exist  
66 exclusively in human SPL and are not observed in rodents or even non-human primates<sup>13,22</sup>.  
67 However, human tissue studies have historically been limited to two-dimensional (2D) tissue

68 cross-sections stained for low-parameter combinations of markers, highlighting the need to  
69 characterize the human SPL and LN using a combination of highly multiplexed 2D and three-  
70 dimensional (3D) modalities.

71

72 **Multiplexed 2D-imaging of immune, lymphatic and blood vessel markers in human SPL  
73 and LN**

74 To extensively profile the cellular architecture of immune cells along with lymphatic and blood  
75 endothelial cells (LECs and BECs, respectively) within the human SPL and LN, antibodies were  
76 first validated by immunohistochemistry (IHC), demonstrating the expected organ-specific  
77 staining patterns within formalin fixed paraffin embedded (FFPE) tissue sections (Extended  
78 Data Fig. 1). SPL and LN tissue sections were then stained with a 29-marker panel  
79 (Supplemental Table 1) for highly multiplexed imaging using CODEX (CO-Detection by  
80 indexing)<sup>23,24</sup>. Visualizing the expression patterns (Extended Data Fig. 2) for immune cell  
81 type/subset-defining markers<sup>25,26</sup> [B cell (CD20, CD21), follicular dendritic cell (FDC; CD21,  
82 CD35), T cell (CD3 $\epsilon$ , CD4, CD8 $\alpha$ , CD45RO), neutrophil (CD15), and macrophage (CD68,  
83 CD163)] delineates the organ-specific structures comprised of repeating functional units (i.e.,  
84 lymphoid follicles). When combined with the endothelial markers [LYVE1, podoplanin (PDPN),  
85 and PROX1 for LECs<sup>25,27</sup>; CD31 and CD34 for BECs<sup>28,29</sup>], one is able to appreciate the intricate  
86 cellular architecture of “normal”/non-diseased LN and SPL (Extended Data Fig. 3-5).

87 Contrary to observations from single cell transcriptomic profiling of murine LN<sup>4,5</sup>, our  
88 results demonstrate that LYVE1 and PDPN expression do not overlap in the human LN or SPL  
89 (Fig. 1). To substantiate these observations, a pair-wise pixel-based Pearson’s correlation  
90 analysis was utilized to generate averaged R values, providing a measure of signal correlation  
91 in LN and SPL (Extended Data Fig. 5e-f). Indeed, the LYVE1/PDPN marker pair had little to no  
92 overlap (LN, R = 0.028; SPL R = 0.0), in contrast with marker pairs such as CD4/CD3 (LN, R =

93 0.69; SPL, R = 0.48) and CD21/CD35 (LN, R = 0.57; SPL, R = 0.61) which were moderately  
94 correlated, as expected<sup>30</sup>.

95 PDPN and smooth muscle actin (SMA) appear to define the LN subcapsular sinus<sup>31</sup>  
96 (SCS), as depicted in Fig. 1a with annotations (inset) of the LN including lymphoid follicles and  
97 lymphatic endothelium<sup>6,31</sup>. Indeed, our results illustrate the expected expression patterns for  
98 LYVE1<sup>32,33</sup>, which identifies the complex network of LN LECs<sup>15,16</sup> (Fig.1a,b,c,d,e). Consistent  
99 with previous studies<sup>34,35</sup>, PDPN+ cells are observed within LN follicles (Fig. 1a,e,f; PDPN/CD21  
100 R = 0.21, PDPN/CD35 R = 0.24, Extended Data Fig. 5e). Within SPL, we are able to visualize  
101 follicles, periarteriolar lymphoid sheath (PALS), trabeculae, and associated trabecular arteries  
102 positioned amongst the intricate network of venous sinuses, as shown in Fig. 1h-i and  
103 annotated within the inset. Interestingly, LYVE1 labels CD8 $\alpha$ + LCs lining the venous  
104 sinusoids<sup>13,36</sup> (Fig. 1j,k). In contrast with LN, PDPN expression is absent in SPL follicles (Fig  
105 1h,l; PDPN/CD21 R = 0.02, PDPN/CD35 R = 0.08, Extended Data Fig. 5f). Finally, PDPN is  
106 observed surrounding large arteries in both organs (Fig. 1a,h), and specifically in splenic  
107 trabeculae (Fig. 1i,m).

108 Vimentin is observed throughout the LN sinuses and endothelium labeled by CD34,  
109 SMA, and CD31 (Fig. 1c,f,g). In the SPL, vimentin partially overlaps with LYVE1 (R = 0.44),  
110 most notably in splenic sinusoids identifying CD8 $\alpha$ + LCs<sup>13</sup> (Fig. 1j). The CD8 $\alpha\beta$  heterodimer is a  
111 canonical T cell marker<sup>37</sup> and as expected, CD8 $\alpha$  labels individual T cells scattered across the  
112 LN (Fig. 1c,d,e and Extended Data Fig. 2b). However, within the SPL, CD8 $\alpha$  also defines the  
113 LCs of the splenic sinuses, in line with previous reports<sup>13</sup>, overlapping with vimentin and LYVE1  
114 (Fig. 1j,k,l). CD107a (lysosome-associated membrane glycoprotein 1 [LAMP1]), which marks  
115 degranulation on Natural Killer (NK) cells and CD8 $+$  T cells<sup>38</sup> along with leukocyte adhesion to  
116 vascular endothelium<sup>39</sup>, and the monocyte/M2 macrophage marker CD163 are observed  
117 throughout the LN sinus network (Fig. 1d,g) while in SPL, both markers localized to the cords of

118 Billroth between venous sinuses within the red pulp (Fig. 1k,n). To corroborate the  
119 representative images in Figure 1, we provide additional CODEX datasets both from  
120 independent donors and within multiple common coordinate framework (CCF)<sup>40,41</sup>-defined tissue  
121 regions for both LN and SPL (Extended Data Fig. 3-5), and complete CODEX datasets are  
122 publicly available on the HuBMAP data portal (Extended Data Table 1).

123

#### 124 **Cell clustering and quantitation in 2D**

125 For a subset of donors, we utilized a 16 marker spatial X-shift clustering<sup>42</sup> to segregate and  
126 classify various cell populations in both LN and SPL (Fig. 2a). We then annotated cell clusters  
127 based on canonical marker expression and tissue localization. As anticipated<sup>43</sup>, T cells account  
128 for approximately one-half of all cells in LN; this, in contrast with approximately 10% of all cells  
129 in SPL. The majority of T cells in either tissue are CD8<sup>+</sup> (Fig. 2b), as expected<sup>44-46</sup>. The CD15<sup>+</sup>  
130 neutrophil population provides a further distinction between the two organs comprising  
131 approximately 1% of cells in LN versus 30% in SPL, which is in line with the literature<sup>47-49</sup>. A  
132 color coordinated Voronoi tessellation image provides a visual illustration of annotated cell  
133 populations organized within and around a follicle in each tissue (Fig. 2c). Specifically, B cells  
134 and FDCs localized within the follicle, surrounded by marginal zone B cells, which were more  
135 pronounced in LN than in SPL, in agreement with prior reports<sup>50</sup>. Follicles were further  
136 surrounded by a distributed mixture of the other cell clusters.

137 We next performed a nonlinear high dimensionality reduction using t-Distributed  
138 Stochastic Neighbor Embedding (t-SNE)<sup>51</sup> to project all clustered populations defined in Fig. 2a  
139 into low-dimensional space (Figs. 2d). Foremost, these renderings highlight the dramatic  
140 differences in T cell and neutrophil population frequencies within the two organs, which is further  
141 illustrated by the gated graphs displaying individual total T cell, B cell, and  
142 neutrophil/macrophage populations in the LN and SPL (Fig. 2e). Fig. 2e (far right) also  
143 demonstrates the proximity of the macrophage population in the cords of Billroth (Fig.1k,n) with

144 the LCs lining the splenic sinuses. Cellular clustering, Voronoi images and global as well as  
145 gated t-SNE images for four additional LN and SPL are provided in Extended Data Figures 6  
146 and 7, respectively.

147

### 148 **3D-imaging of perivascular innervation in SPL and LN**

149 To visualize vascular innervation of the human LN and SPL in 3D, we employed multiplexed,  
150 three-color light sheet fluorescence microscopy (LSFM)<sup>52,53</sup> on tissues cleared using CLARITY-  
151 based methodology<sup>54,55</sup>. An example of a pre- and post-cleared intact human LN is shown in  
152 Extended Data Figure 8a. Extensive 3D perivascular innervation is observed on CD31+  
153 endothelial cells within vessels of human LN (Fig. 3a-d) and SPL (Fig. 3e-h). CD31 specificity is  
154 visualized at the individual endothelial cell level in the SPL (Extended Data Fig. 8b,c). Staining  
155 with the pan-neuronal marker PGP9.5 reveals a complex matrix of neural processes  
156 surrounding CD31+ vasculature of the LN (Fig. 3b-d) and SPL (Fig. 3f-h) located within the *nervi*  
157 *vasorum* of the *tunica externa* layer<sup>56</sup> of the vessel wall (Extended Data Fig. 8d). *Nervi vasorum*  
158 staining is also observed in SPL for the peripheral sympathetic neuronal marker tyrosine  
159 hydroxylase (TH) (Extended Data Fig. 8e, Supplemental Video 1). Interestingly, choline  
160 acetyltransferase (ChAT), an enzyme required for production of the neurotransmitter  
161 acetylcholine within parasympathetic neurons<sup>57</sup>, colocalizes with a subset of the PGP9.5+  
162 perivascular axons in the LN (Fig. 3a-d) and SPL (Fig. 3e-h). This is in contrast with the  
163 previous literature<sup>58</sup>, including recent IHC data from human cadaveric specimens where  
164 PGP9.5<sup>+</sup> staining was documented in the absence of ChAT<sup>7</sup> as well as 3D imaging of cleared  
165 SPL from mice where ChAT<sup>+</sup> nerve fibers were not detected<sup>59</sup>. However, our intensity-based  
166 volumetric segmentation demonstrates that 21% of the PGP9.5+ neuronal processes also  
167 contain ChAT in the LN evaluated, and similarly, 22% contain ChAT in SPL (Fig. 3c,g).  
168 Renderings of sequential optical slices through the Z dimension provide 3D visualization of  
169 perivascular innervation within human LN (Supplemental Video 2) and SPL (Supplemental

170 Video 3), demonstrating that PGP9.5, ChAT, and TH primarily label neuronal processes on  
171 large vessels in both organs.

172 LSFM imaging of LN further identifies perivascular innervation of large vessels  
173 expressing the pan-neuronal marker  $\beta$ 3-tubulin as well as an extensive mesh-like vessel  
174 network expressing both  $\beta$ 3-tubulin and neuronal growth-associated protein (GAP43, or  
175 neuromodulin)<sup>15,16,60,61</sup> (Fig. 4a-c; Supplemental Video 4). Indeed, in comparison to 2D analysis,  
176 LSFM affords the ability to better appreciate these complex structures in 3D. Indeed, in  
177 Extended Data Fig. 9a, we provide a close examination of high-resolution 3D max-projection  
178 images. We also observe  $\beta$ 3-tubulin+ nerve bundles adjacent to blood vessels (Fig. 4b;  
179 Supplemental Video 5), along with a single GAP43<sup>+</sup> axon within a vessel labeled by  $\beta$ 3-tubulin  
180 (Extended Data Fig. 9b).

181 As expected, the leukocyte marker Coronin-1A<sup>62</sup> is detected throughout the LN (Fig. 4a-  
182 c; Supplemental Video 5). In contrast, Coronin-1A expression is less homogenous in SPL,  
183 observed both on single cells and on cells clustered around large vascular structures identified  
184 by perivascular nerves expressing  $\beta$ 3-tubulin (Fig. 4e). Within the SPL,  $\beta$ 3-tubulin identifies  
185 large vascular processes, whereas GAP43 identifies both large and small vessels (Fig. 4e-i),  
186 corresponding either to BEC or efferent LECs<sup>63</sup>. Interestingly, immunolabeling with GAP43  
187 demonstrated staining localized to the internal elastic membrane or smooth muscle layer of  
188 large blood vessels in both LN (Fig. 4d) and SPL (Fig. 4h). These GAP43 data clearly define  
189 filamentous neuronal processes existing on the internal aspect of large vessels (Extended Data  
190 Fig. 8d), unexpected from conventional *nervi vasorum* location of vascular innervation<sup>7</sup>. To our  
191 knowledge, this localization of GAP43 expressing cells has not previously been reported in  
192 human LN or SPL vessels.

193

#### 194 **Differential expression of perivascular GAP43 and $\beta$ 3-tubulin in LN and SPL**

195 A detailed review of our 3D LSFM data reveals a novel observation involving differential

196 expression of  $\beta$ 3-tubulin and GAP43 along discrete segments of large vessels in both LN and  
197 SPL (Fig. 5a-g). Specifically, within LN, select segments of large vessels display a reduction or  
198 absence of protein expression for either GAP43 (Fig. 5a) or  $\beta$ 3-tubulin (Fig. 5b,c) as quantified  
199 using an intensity-based volumetric segmentation (Extended Data Fig. 10a,b).

200 Similarly, GAP43 protein expression is notably diminished along segments of large  
201 vessels within the SPL, in the context of contiguous  $\beta$ 3-tubulin expression (Fig. 5d,e). Figure 5d  
202 also reaffirms the observation that within the SPL, GAP43 detects neuronal elements on both  
203 large and small vessels, while  $\beta$ 3-tubulin is primarily found on cells along large vessels (Fig.  
204 4e,i). Notably, diminished expression of GAP43 along segments of large vessels in the SPL  
205 appears to associate with densely clustered populations of Coronin-1A+ cells (Fig. 5f,g,  
206 Supplemental Video 6), as supported by quantitative volumetric segmentation (Extended Data  
207 Fig. 10c,d). To further this observation, we utilized CODEX to examine a region of the SPL that  
208 included a PALS with CD45RO+ T cells surrounding blood vessels (Fig. 5h and Extended Data  
209 Fig. 11) and noted that these T cell clusters may potentially correspond to the Coronin-1A+ cells  
210 observed in LSFM.

211

## 212 **Discussion**

213 Herein we provide novel 2D and 3D characterization of the immune, endothelial, and neuronal  
214 cell networks within the normal human LN and SPL. Among key observations, LYVE1 and  
215 PDPN do not overlap in either tissue, as supported by pairwise pixel-based quantitation.  
216 Specifically, PDPN and SMA label the LN subcapsular sinus with LYVE1 also staining the  
217 lymphatic endothelium within the LN interior. Importantly, studies using a PDPN+ cell sorting  
218 strategy to isolate LEC from murine LN prior to single cell transcriptomics, may fail to observe  
219 the LYVE1+ population of cells<sup>4,5</sup>. Building on a seminal studies of LCs<sup>13</sup> and endothelial cells<sup>27</sup>,  
220 we report that LYVE1 labels LCs lining the SPL sinusoids, along with vimentin and CD8a, while

221 PDPN is expressed in central arteries and trabeculae. LCs do not exist in rodents or non-human  
222 primates, emphasizing the importance of performing these cell mapping studies in human  
223 tissue<sup>13</sup>. The abundance of macrophages expressing CD163 (hemoglobin scavenger receptor)  
224 within the splenic cords of Billroth is in line with the existing literature and supports this organ's  
225 well-established function as the primary site for filtration of aged or damaged red blood cells  
226 from circulation<sup>13,64</sup>. Neighborhood analysis using our CODEX data, coupled with population cell  
227 counts, delineates the disparate composition of T cell and CD15+ neutrophil populations in the  
228 LN versus the SPL, in line with prior reports<sup>44-49</sup>. In particular, we observe a much higher  
229 proportion of CD3+CD8a+ T cells in the LN compared with SPL. In addition, we note a smaller  
230 population of CD15+ neutrophils in the LN versus the SPL, corroborating the existing  
231 literature<sup>65,66</sup>.

232 Our LSF data highlight the power and utility of 3D imaging to observe intact tissue  
233 volumes, consisting of thousands of optical sections from any vantage point, providing new  
234 insights into human tissue organization that may be masked by max projection, single-section  
235 2D views, or 3D stitching of 2D images. This effort, which applied three-color  
236 immunofluorescent staining to human secondary lymphoid organs, represents an advance on  
237 prior LSF imaging studies<sup>52,53,67-69</sup>. Moreover, given HuBMAP's use of a CCF<sup>40,41</sup>, the images  
238 presented herein can be mapped back to their physical location within the intact organ. Within  
239 both LN and SPL, the PGP9.5,  $\beta$ 3-tubulin, ChAT, and TH markers identify an extensive network  
240 of perivascular neuronal processes localized to the *nervi vasorum* of the *tunica externa*, while  
241 GAP43 appears to localize to the internal elastic membrane or smooth muscle layers of the  
242 artery<sup>70</sup>. We further observe that nerves expressing GAP43 and  $\beta$ 3-tubulin associate with an  
243 extensive network of small vessels within the LN. Moving forward, there is a need to corroborate  
244 our interpretation that LN LYVE1 staining, visualized in 2D via CODEX, may correspond with  
245 this vessel network.

246 The leukocyte marker Coronin-1A identifies scattered single cells in LN imaged by  
247 LSFM. In contrast, Coronin-1A+ cells are both scattered and clustered around vascular  
248 structures in SPL. Interestingly, accumulation of leukocytes around SPL blood vessels (PALS)  
249 appears associated with reduced expression of GAP43. In support of this observation, 2D SPL  
250 CODEX images reveal similar clustering of CD4+ T cells in PALS. Future work will require  
251 functional assays to determine if regions lacking GAP43 correspond to sites for neurovascular  
252 regulation of immune cell extravasation and navigation<sup>71,72</sup>.

253 The data presented herein showcase the unique staining patterns of immune,  
254 endothelial, and neural markers within human secondary lymphoid organs. Given that most  
255 human immune responses occur in secondary lymphatic organs and not peripheral blood<sup>30</sup>,  
256 there is a clear need for additional studies using human tissues to gain insights on how  
257 neuroimmune interactions modulate cellular activity across the lymphatic system. Importantly,  
258 the current 3D cell mapping effort, together with complementary datasets and tools generated  
259 across the HuBMAP Consortium<sup>41,73-77</sup>, among others (e.g., Human Cell Atlas<sup>78</sup>), also set the  
260 stage for future studies to determine how these pathways may be dysregulated in various  
261 disease settings, including autoimmunity, sepsis, cancer, and viral infection. We envision that  
262 novel therapies targeting the neurovascular sites identified herein could potentially be  
263 developed to specifically modulate immune function within the human SPL and LN.

264 **Main References**

265 1 Krishnamurty, A. & Turley, S. Lymph node stromal cells: cartographers of the immune  
266 system. *Nature Immunology* **21**, 369-380 (2020). <https://doi.org/10.1038/s41590-020-0635-3>

267 2 Bronte, V. & Pittet, M. The spleen in local and systemic regulation of immunity. *Immunity*  
268 **39**, 806-818 (2013). <https://doi.org/10.1016/j.immuni.2013.10.010>

269 3 HuBMAP Consortium. The human body at cellular resolution: the NIH Human  
270 Biomolecular Atlas Program. *Nature* **574**, 187-192 (2019).  
<https://doi.org/10.1038/s41586-019-1629-x>

271 4 Fujimoto, N. *et al.* Single-cell mapping reveals new markers and functions of lymphatic  
272 endothelial cells in lymph nodes. *PLoS Biology* **18**, e3000704 (2020).  
<https://doi.org/10.1371/journal.pbio.3000704>

273 5 Berendam, S. *et al.* Comparative Transcriptomic Analysis Identifies a Range of  
274 Immunologically Related Functional Elaborations of Lymph Node Associated Lymphatic  
275 and Blood Endothelial Cells. *Frontiers in Immunology* **10**, 816 (2019).  
<https://doi.org/10.3389/fimmu.2019.00816>

276 6 Louie, D. & Liao, S. Lymph Node Subcapsular Sinus Macrophages as the Frontline of  
277 Lymphatic Immune Defense. *Frontiers in Immunology* **10**, 347 (2019).  
<https://doi.org/10.3389/fimmu.2019.00347>

278 7 Verlinden, T. *et al.* Innervation of the human spleen: A complete hilum-embedding  
279 approach. *Brain, Behavior, and Immunity* **77** (2019).  
<https://doi.org/10.1016/j.bbi.2018.12.009>

280 8 Betterman, K. L. & Harvey, N. L. The lymphatic vasculature: development and role in  
281 shaping immunity. *Immunol Rev* **271**, 276-292 (2016). <https://doi.org/10.1111/imr.12413>

282 9 Randolph, G. J., Ivanov, S., Zinselmeyer, B. H. & Scallan, J. P. The Lymphatic System:  
283 Integral Roles in Immunity. *Annu Rev Immunol* **35**, 31-52 (2017).  
<https://doi.org/10.1146/annurev-immunol-041015-055354>

284 10 Bachmann, S. B. *et al.* A Distinct Role of the Autonomic Nervous System in Modulating  
285 the Function of Lymphatic Vessels under Physiological and Tumor-Draining Conditions.  
*Cell Rep* **27**, 3305-3314 e3313 (2019). <https://doi.org/10.1016/j.celrep.2019.05.050>

286 11 Xiang, M. *et al.* A Single-Cell Transcriptional Roadmap of the Mouse and Human Lymph  
287 Node Lymphatic Vasculature. *Front Cardiovasc Med* **7**, 52 (2020).  
<https://doi.org/10.3389/fcvm.2020.00052>

288 12 Steiniger, B., Timphus, E. M. & Barth, P. J. The splenic marginal zone in humans and  
289 rodents: an enigmatic compartment and its inhabitants. *Histochem Cell Biol* **126**, 641-  
290 648 (2006). <https://doi.org/10.1007/s00418-006-0210-5>

291 13 Ogumbo, J. G. *et al.* SIRPalpha/CD172a and FHOD1 are unique markers of littoral cells,  
292 a recently evolved major cell population of red pulp of human spleen. *J Immunol* **188**,  
293 4496-4505 (2012). <https://doi.org/10.4049/jimmunol.1103086>

294 14 Cleypool, C. *et al.* Age-Related Variation in Sympathetic Nerve Distribution in the Human  
295 Spleen. *Frontiers in Neuroscience* **15**, 726825 (2021).  
<https://doi.org/10.3389/fnins.2021.726825>

296 15 Kelch, I. D. *et al.* High-resolution 3D imaging and topological mapping of the lymph node  
297 conduit system. *PLoS Biol* **17**, e3000486 (2019).  
<https://doi.org/10.1371/journal.pbio.3000486>

298 16 Novkovic, M., Onder, L., Bocharov, G. & Ludewig, B. Topological Structure and  
299 Robustness of the Lymph Node Conduit System. *Cell Rep* **30**, 893-904 e896 (2020).  
<https://doi.org/10.1016/j.celrep.2019.12.070>

312 17 Fletcher, A., Acton, S. & Knoblich, K. Lymph node fibroblastic reticular cells in health and  
313 disease. *Nature Reviews Immunology* **15**, 350-361 (2015).  
<https://doi.org/10.1038/nri3846>

314 18 Huang, S. et al. Lymph nodes are innervated by a unique population of sensory neurons  
315 with immunomodulatory potential. *Cell* **184**, 441-459.e425 (2021).  
<https://doi.org/10.1016/j.cell.2020.11.028>

316 19 Sixt, M. et al. The conduit system transports soluble antigens from the afferent lymph to  
317 resident dendritic cells in the T cell area of the lymph node. *Immunity* **22**, 19-29 (2005).  
<https://doi.org/10.1016/j.immuni.2004.11.013>

318 20 Reynoso, G. V. et al. Lymph node conduits transport virions for rapid T cell activation.  
319 *Nat Immunol* **20**, 602-612 (2019). <https://doi.org/10.1038/s41590-019-0342-0>

320 21 Rozendaal, R., Mebius, R. & Kraal, G. The conduit system of the lymph node.  
321 *International Immunology* **20**, 1483-1487 (2008). <https://doi.org/10.1093/intimm/dxn110>

322 22 Buckley, P. J., Dickson, S. A. & Walker, W. S. Human splenic sinusoidal lining cells  
323 express antigens associated with monocytes, macrophages, endothelial cells, and T  
324 lymphocytes. *J Immunol* **134**, 2310-2315 (1985).

325 23 Goltsev, Y. et al. Deep Profiling of Mouse Splenic Architecture with CODEX Multiplexed  
326 Imaging. *Cell* **174**, 968-981 e915 (2018). <https://doi.org/10.1016/j.cell.2018.07.010>

327 24 Schurch, C. M. et al. Coordinated Cellular Neighborhoods Orchestrate Antitumoral  
328 Immunity at the Colorectal Cancer Invasive Front. *Cell* **182**, 1341-1359 e1319 (2020).  
<https://doi.org/10.1016/j.cell.2020.07.005>

329 25 Kong, L. L. et al. The optimum marker for the detection of lymphatic vessels. *Mol Clin  
330 Oncol* **7**, 515-520 (2017). <https://doi.org/10.3892/mco.2017.1356>

331 26 Ribatti, D., Tamma, R., Ruggieri, S., Annese, T. & Crivellato, E. Surface markers: An  
332 identity card of endothelial cells. *Microcirculation* **27**, e12587 (2020).  
<https://doi.org/10.1111/micc.12587>

333 27 Breiteneder-Geleff, S. et al. Angiosarcomas express mixed endothelial phenotypes of  
334 blood and lymphatic capillaries: podoplanin as a specific marker for lymphatic  
335 endothelium. *The American Journal of Pathology* **154**, 385-394 (1999).  
[https://doi.org/10.1016/S0002-9440\(10\)65285-6](https://doi.org/10.1016/S0002-9440(10)65285-6)

336 28 Lertkiatmongkol, P., Liao, D., Mei, H., Hu, Y. & Newman, P. J. Endothelial functions of  
337 platelet/endothelial cell adhesion molecule-1 (CD31). *Curr Opin Hematol* **23**, 253-259  
338 (2016). <https://doi.org/10.1097/MOH.0000000000000239>

339 29 Fina, L. et al. Expression of the CD34 gene in vascular endothelial cells. *Blood* **75**, 2417-  
340 2426 (1990).

341 30 Kumar, B., Connors, T. & Farber, D. Human T Cell Development, Localization, and  
342 Function throughout Life. *Immunity* **48**, 202-213 (2018).  
<https://doi.org/10.1016/j.immuni.2018.01.007>

343 31 Jalkanen, S. & Salmi, M. Lymphatic endothelial cells of the lymph node. *Nat Rev  
344 Immunol* **20**, 566-578 (2020). <https://doi.org/10.1038/s41577-020-0281-x>

345 32 Park, S. et al. Mapping the distinctive populations of lymphatic endothelial cells in  
346 different zones of human lymph nodes. *PLoS one* **9**, e94781 (2014).  
<https://doi.org/10.1371/journal.pone.0094781>

347 33 Jackson, D. The lymphatics revisited: new perspectives from the hyaluronan receptor  
348 LYVE-1. *Trends in Cardiovascular Medicine* **13**, 1-7 (2003).  
[https://doi.org/10.1016/s1050-1738\(02\)00189-5](https://doi.org/10.1016/s1050-1738(02)00189-5)

349 34 Marsee, D., Pinkus, G. & Hornick, J. Podoplanin (D2-40) is a highly effective marker of  
350 follicular dendritic cells. *Applied immunohistochemistry & molecular morphology : AIMM*  
351 **17**, 102-107 (2009). <https://doi.org/10.1097/PAI.0b013e318183a8e2>

361 35 Xie, Q. *et al.* Podoplanin (d2-40): a new immunohistochemical marker for reactive  
362 follicular dendritic cells and follicular dendritic cell sarcomas. *International journal of*  
363 *clinical and experimental pathology* **1**, 276-284 (2008).

364 36 Steiniger, B., Stachniss, V., Schwarzbach, H. & Barth, P. J. Phenotypic differences  
365 between red pulp capillary and sinusoidal endothelia help localizing the open splenic  
366 circulation in humans. *Histochem Cell Biol* **128**, 391-398 (2007).  
<https://doi.org:10.1007/s00418-007-0320-8>

368 37 Reina-Campos, M., Scharping, N. E. & Goldrath, A. W. CD8(+) T cell metabolism in  
369 infection and cancer. *Nat Rev Immunol* (2021). <https://doi.org:10.1038/s41577-021-00537-8>

371 38 Aktas, E., Kucuksezer, U., Bilgic, S., Erten, G. & Deniz, G. Relationship between  
372 CD107a expression and cytotoxic activity. *Cellular Immunology* **254**, 149-154 (2009).  
<https://doi.org:10.1016/j.cellimm.2008.08.007>

374 39 Kannan, K. *et al.* Lysosome-associated membrane proteins h-LAMP1 (CD107a) and h-  
375 LAMP2 (CD107b) are activation-dependent cell surface glycoproteins in human  
376 peripheral blood mononuclear cells which mediate cell adhesion to vascular  
377 endothelium. *Cellular Immunology* **171**, 10-19 (1996).  
<https://doi.org:10.1006/cimm.1996.0167>

379 40 Rood, J. *et al.* Toward a Common Coordinate Framework for the Human Body. *Cell* **179**,  
380 1455-1467 (2019). <https://doi.org:10.1016/j.cell.2019.11.019>

381 41 Weber, G., Ju, Y. & Börner, K. Considerations for Using the Vasculature as a Coordinate  
382 System to Map All the Cells in the Human Body. *Frontiers in Cardiovascular Medicine* **7**,  
383 29 (2020). <https://doi.org:10.3389/fcvm.2020.00029>

384 42 Samusik, N., Good, Z., Spitzer, M., Davis, K. & Nolan, G. Automated mapping of  
385 phenotype space with single-cell data. *Nature Methods* **13**, 493-496 (2016).  
<https://doi.org:10.1038/nmeth.3863>

387 43 Bousso, P. T-cell activation by dendritic cells in the lymph node: lessons from the  
388 movies. *Nature Reviews Immunology* **8**, 675-684 (2008). <https://doi.org:10.1038/nri2379>

389 44 Poppema, S., Bhan, A., Reinherz, E., McCluskey, R. & Schlossman, S. Distribution of T  
390 cell subsets in human lymph nodes. *The Journal of Experimental Medicine* **153**, 30-41  
391 (1981). <https://doi.org:10.1084/jem.153.1.30>

392 45 Sathaliyawala, T. *et al.* Distribution and compartmentalization of human circulating and  
393 tissue-resident memory T cell subsets. *Immunity* **38**, 187-197 (2013).  
<https://doi.org:10.1016/j.immuni.2012.09.020>

395 46 Langeveld, M., Gamadia, L. & ten Berge, I. T-lymphocyte subset distribution in human  
396 spleen. *European Journal of Clinical Investigation* **36**, 250-256 (2006).  
<https://doi.org:10.1111/j.1365-2362.2006.01626.x>

398 47 Puga, I. *et al.* B cell-helper neutrophils stimulate the diversification and production of  
399 immunoglobulin in the marginal zone of the spleen. *Nature Immunology* **13**, 170-180  
400 (2011). <https://doi.org:doi:10.1038/ni.2194>

401 48 Meinderts, S. *et al.* Human and murine splenic neutrophils are potent phagocytes of IgG-  
402 opsonized red blood cells. *Blood Advances* **1**, 875-886 (2017).  
<https://doi.org:10.1182/bloodadvances.2017004671>

404 49 Lok, L. *et al.* Phenotypically distinct neutrophils patrol uninfected human and mouse  
405 lymph nodes. *Proceedings of the National Academy of Sciences of the United States of*  
406 *America* **116**, 19083-19089 (2019). <https://doi.org:10.1073/pnas.1905054116>

407 50 Palm, A. & Kleinau, S. Marginal zone B cells: From housekeeping function to  
408 autoimmunity? *Journal of Autoimmunity* **119**, 102627 (2021).  
<https://doi.org:10.1016/j.jaut.2021.102627>

410 51 van der Maaten, L. & Hinton, G. Visualizing Data using t-SNE. *Journal of Machine*  
411 *Learning Research* **9**, 2579-2605 (2008).

412 52 Power, R. M. & Huisken, J. A guide to light-sheet fluorescence microscopy for multiscale  
413 imaging. *Nat Methods* **14**, 360-373 (2017). <https://doi.org/10.1038/nmeth.4224>

414 53 Wan, Y., McDole, K. & Keller, P. J. Light-Sheet Microscopy and Its Potential for  
415 Understanding Developmental Processes. *Annu Rev Cell Dev Biol* **35**, 655-681 (2019).  
<https://doi.org/10.1146/annurev-cellbio-100818-125311>

416 54 Chung, K. *et al.* Structural and molecular interrogation of intact biological systems.  
417 *Nature* **497**, 332-337 (2013). <https://doi.org/10.1038/nature12107>

418 55 Gradinaru, V., Treweek, J., Overton, K. & Deisseroth, K. Hydrogel-Tissue Chemistry:  
419 Principles and Applications. *Annu Rev Biophys* **47**, 355-376 (2018).  
<https://doi.org/10.1146/annurev-biophys-070317-032905>

420 56 *Structure and Function of Blood Vessels | Anatomy and Physiology II*,  
421 <<https://courses.lumenlearning.com/suny-ap2/chapter/structure-and-function-of-blood-vessels/>> (

422 57 Bellier, J. & Kimura, H. Peripheral type of choline acetyltransferase: biological and  
423 evolutionary implications for novel mechanisms in cholinergic system. *J Chem  
424 Neuroanat* **42**, 225-235 (2011). <https://doi.org/10.1016/j.jchemneu.2011.02.005>

425 58 Nance, D. & Sanders, V. Autonomic innervation and regulation of the immune system  
426 (1987-2007). *Brain, Behavior, and Immunity* **21**, 736-745 (2007).  
<https://doi.org/10.1016/j.bbi.2007.03.008>

427 59 Ding, X. *et al.* Panicle-Shaped Sympathetic Architecture in the Spleen Parenchyma  
428 Modulates Antibacterial Innate Immunity. *Cell Reports* **27**, 3799-3807.e3793 (2019).  
<https://doi.org/10.1016/j.celrep.2019.05.082>

429 60 Shaikh, H. *et al.* Mesenteric Lymph Node Transplantation in Mice to Study Immune  
430 Responses of the Gastrointestinal Tract. *Frontiers in Immunology* **12**, 689896 (2021).  
<https://doi.org/10.3389/fimmu.2021.689896>

431 61 Matryba, P. *et al.* Systematic Evaluation of Chemically Distinct Tissue Optical Clearing  
432 Techniques in Murine Lymph Nodes. *Journal of Immunology* **204**, 1395-1407 (2020).  
<https://doi.org/10.4049/jimmunol.1900847>

433 62 Ferrari, G., Langen, H., Naito, M. & Pieters, J. A coat protein on phagosomes involved in  
434 the intracellular survival of mycobacteria. *Cell* **97**, 435-447 (1999).  
[https://doi.org/10.1016/s0092-8674\(00\)80754-0](https://doi.org/10.1016/s0092-8674(00)80754-0)

435 63 Mebius, R. E. & Kraal, G. Structure and function of the spleen. *Nat Rev Immunol* **5**, 606-  
436 616 (2005). <https://doi.org/10.1038/nri1669>

437 64 Nagelkerke, S. *et al.* Red pulp macrophages in the human spleen are a distinct cell  
438 population with a unique expression of Fc-γ receptors. *Blood Advances* **2**, 941-953  
439 (2018). <https://doi.org/10.1182/bloodadvances.2017015008>

440 65 Jakovija, A. & Chtanova, T. Neutrophil Interactions with the Lymphatic System. *Cells* **10**,  
441 2106 (2021). <https://doi.org/10.3390/cells10082106>

442 66 Maletto, B. *et al.* Presence of neutrophil-bearing antigen in lymphoid organs of immune  
443 mice. *Blood* **108**, 3094-3102 (2006). <https://doi.org/10.1182/blood-2006-04-016659>

444 67 Luna-Palacios, Y. *et al.* Multicolor light-sheet microscopy for a large field of view  
445 imaging: A comparative study between Bessel and Gaussian light-sheets configurations.  
446 *Journal of Biophotonics* **15**, e202100359 (2022). <https://doi.org/10.1002/jbio.202100359>

447 68 Schoppmeyer, R., Zhao, R., Hoth, M. & Qu, B. Light-sheet Microscopy for Three-  
448 dimensional Visualization of Human Immune Cells. *Journal of Visualized Experiments*,  
449 57651 (2018). <https://doi.org/10.3791/57651>

450 69 Dekkers, J. F. *et al.* High-resolution 3D imaging of fixed and cleared organoids. *Nature  
451 Protocols* **14**, 1756-1771 (2019). <https://doi.org/doi:10.1038/s41596-019-0160-8>

452 70 Yang, H., Wang, L., Huang, C. & Ju, G. Plasticity of GAP-43 innervation of the spleen  
453 during immune response in the mouse. Evidence for axonal sprouting and redistribution

462 of the nerve fibers. *Neuroimmunomodulation* **5**, 53-60 (1998).  
463 <https://doi.org/10.1159/000026326>

464 71 Stark, K. *et al.* Capillary and arteriolar pericytes attract innate leukocytes exiting through  
465 venules and 'instruct' them with pattern-recognition and motility programs. *Nature  
466 Immunology* **14**, 41-51 (2013). <https://doi.org/10.1038/ni.2477>

467 72 Iadecola, C. The Neurovascular Unit Coming of Age: A Journey through Neurovascular  
468 Coupling in Health and Disease. *Neuron* **96**, 17-42 (2017).  
469 <https://doi.org/10.1016/j.neuron.2017.07.030>

470 73 Hao, Y. *et al.* Integrated analysis of multimodal single-cell data. *Cell* **184**, 3573-  
471 3587.e3529 (2021). <https://doi.org/10.1016/j.cell.2021.04.048>

472 74 Missarova, A. *et al.* geneBasis: an iterative approach for unsupervised selection of  
473 targeted gene panels from scRNA-seq. *Genome Biol* **22**, 333 (2021).  
474 <https://doi.org/10.1101/2021.08.10.455720>

475 75 Bueckle, A., Buehling, K., Shih, P. & Börner, K. 3D virtual reality vs. 2D desktop  
476 registration user interface comparison. *PLoS One* **16**, e0258103 (2021).  
477 <https://doi.org/10.1371/journal.pone.0258103>

478 76 Hasanaj, E., Wang, J., Sarathi, A., Ding, J. & Bar-Joseph, Z. Interactive single-cell data  
479 analysis using Cellar. *Nature Communications* **13**, 1998 (2022).  
480 <https://doi.org/10.1038/s41467-022-29744-0>

481 77 Börner, K. *et al.* Anatomical structures, cell types and biomarkers of the Human  
482 Reference Atlas. *Nature Cell Biology* **23**, 1117-1128 (2021).  
483 <https://doi.org/doi:10.1038/s41556-021-00788-6>

484 78 Regev, A. *et al.* The Human Cell Atlas. *eLife* **6**, e27041 (2017).  
485 <https://doi.org/10.7554/eLife.27041>

486

487 **Figures**

488

489 **Figure 1. Immune, LEC, BEC, and stromal cell organization in human LN and SPL.**

490 Representative CODEX images of **a-g**, LN and **i-n**, SPL. **a**, LN cross-section (scale bar 690 $\mu$ m) with annotated inset (scale bar 180 $\mu$ m) showing capsule, subcapsular sinus (SCS), follicles (Fo; CD21+PDPN+), and lymphatic endothelium within the sinus (LYVE1+). The LN showed normal microarchitecture with respect to sinus distribution and follicular meshwork formation. **b**, CD31+CD34+SMA+ high endothelial venule (HEV, white arrow) within the LYVE1+ sinus along with PDPN+ veins (white arrowheads). **c**, CD4+ (left) and CD8a+ (right) interfollicular T cell zone with Vimentin+ stroma. **d**, CD107a cytotoxic lymphocytes and CD163 macrophages within the interfollicular space. **e**, CD20+ B cells enrich the PDPN+ follicular dendritic cell (FDC) meshwork within a Fo with CD8a identifying the T cells within the interfollicular space along with CD163+ macrophages. **f**, CD20+ B cells enrich the PDPN+ Fo with SMA highlighting proximal arteries and CD34 highlighting venules. Vimentin illustrates background stromal architecture. **g**, CD20 identifies a Fo with CD163 highlighting interfollicular macrophages and with SMA, Vimentin, and CD31 highlighting stroma and endothelium. **h**, SPL cross-section (scale bar 690 $\mu$ m) with annotated inset (scale bar 180 $\mu$ m) showing CD21+PDPN- Fo, LYVE1+ venous sinusoids (Sinus), with CD31+CD34+SMA+PDPN+ highlighting the arterioles and periafteriolar lymphoid sheaths (PALS). **i**, CD34+PDPN+SMA+ trabecula surrounded by LYVE1+ venous sinusoids. **j**, CD4+ T cells (left) within the cords of Billroth; CD8a+ LCs with LYVE1+ lymphatic endothelium and LYVE1-CD8a+ T cells within the cords of Billroth (right). **k**, Cords of Billroth with CD107a+, CD8a+/- cytotoxic lymphocytes and CD163+ macrophages arranged between the CD8a+ LCs and LYVE1+ sinusoidal lymphatic endothelium. **l**, CD20+PDPN- Fo surrounded by CD8a+ LC and LYVE1+ sinusoidal lymphatic endothelium with CD163+ macrophages in the cords of Billroth. **m**, SMA+CD34+ trabecula with Vimentin+ highlighting background stroma and only rare CD20+ B cells and absence of PDPN+ FDCs. **n**, White pulp with tangentially sectioned

513 CD20+ Fo and adjacent SMA+ PALS. Vimentin highlights stroma and CD163+ macrophages in  
514 cords of Billroth. **b-g and i-n**, Scale bars, 180 $\mu$ m. Donor ID, tissue, and region defined to the  
515 right of each panel.

516

517 **Figure 2. Cell clustering, segmentation, and t-SNE visualization.** Analysis of CODEX data  
518 from LN (*left*, n=5) and SPL (*right*, n=5) with identical color coding for each cluster throughout  
519 and Littoral cells included as an additional cluster for SPL. **a**, Supervised X-shift clustering with  
520 heatmap illustrating protein markers that define each cluster and cell counts for each cluster  
521 with donor IDs in upper left corner. **b**, Cell counts for each supervised cluster are plotted as the  
522 percent of the total cell population for each donor image. **c**, Clustered Voronoi plot of follicles  
523 prominently highlighting the three supervised B cell populations in the LN and SPL. **d**, Global  
524 high dimensionality reduction of clustered data set using t-SNE (t-Distributed Stochastic  
525 Neighbor Embedding). **e** Three gated t-SNE plots for T (upper), B (middle), as well as  
526 neutrophil, macrophage, and/or Littoral cell (lower) populations. Analyses performed with Akoya  
527 CODEXMaV plugin to NIH Fiji using default algorithm parameters.

528

529 **Figure 3. Perivascular innervation of human LN and SPL imaged with 3D LSF.** Multicolor  
530 LSF imaging of CD31+ vessels with ChAT and PGP9.5 innervation in **a-d**, LN and **e-h**, SPL.  
531 **a, e**, 3D renderings of 0.5 mm<sup>3</sup> (LN) and 1 mm<sup>3</sup> (SPL) tissue volumes. **b, f**, Max intensity  
532 projection of vessels expressing CD31 surrounded by extensive PGP9.5-positive innervation  
533 with partial ChAT-positive neuronal processes in LN (100  $\mu$ m) and SPL (50  $\mu$ m). **c, g**, 3D  
534 renderings of perivascular neuronal network illustrating a subset of ChAT+ axons with the  
535 percent of total PGP9.5+ axons expressing ChAT determined using semi-automated, intensity-  
536 based volumetric segmentation with the Arivis software package. **d, h**, Cross-section through  
537 LN (50  $\mu$ m) and SPL vessels (10  $\mu$ m) demonstrating co-localization of ChAT and PGP9.5 neural  
538 components within the *tunica externa*. Donor ID, tissue, and region are defined at the top.

539

540 **Figure 4. Neural markers along vessels of human LN and SPL.** Multicolor LSFM imaging of  
541  $\beta$ 3-tubulin and GAP43 innervation with Coronin-1A+ leukocytes in **a-d**, LN and **e-i**, SPL. **a**, 3D  
542 rendering of 0.5 mm<sup>3</sup> LN tissue. **b**, Max intensity projection (*left*) of LN large vessel and nerve  
543 bundles expressing  $\beta$ 3-tubulin woven between an extensive  $\beta$ 3-tubulin+GAP43+ small vessel  
544 network (100  $\mu$ m) with inset showing zoomed in cross-section (*right*) with blood vessel diameter  
545 annotated (60  $\mu$ m). **c**, Wide-field max intensity projection showing Coronin-1A+ leukocytes  
546 among a complex network of  $\beta$ 3-tubulin+GAP43+ small diameter vessels (100  $\mu$ m). **d**, LN  
547 vessel cross-section demonstrating localization of  $\beta$ 3-tubulin to the *tunica externa* and GAP43 to  
548 the *tunica interna* of the vascular wall (50  $\mu$ m). **e**, 3D rendering of 1 mm<sup>3</sup> SPL tissue. **f**, **g**, Max  
549 intensity projection of SPL vessels expressing  $\beta$ 3-tubulin within the wall and GAP43 within the  
550 internal lining (20  $\mu$ m). **h**, Max intensity projection showing  $\beta$ 3-tubulin+GAP43+ large and  
551 GAP43+ small vessels (100  $\mu$ m). **i**, SPL vessel cross-section demonstrating localization of  $\beta$ 3-  
552 tubulin to the *tunica externa* and GAP43 to the *tunica interna* of the vascular wall (20  $\mu$ m).  
553 Donor ID, tissue, and region are defined at the top.

554

555 **Figure 5. Differential expression of  $\beta$ 3-tubulin and GAP43 along discrete segments of**  
556 **large blood vessels in human LN and SPL.** Multicolor LSFM imaging of  $\beta$ 3-tubulin and  
557 GAP43 innervation in LN (**a-c**) and SPL with Coronin-1A+ leukocytes (**d-g**). **a**, Max intensity  
558 projection showing large  $\beta$ 3-tubulin+ vascular segment with a region of decreased GAP43  
559 expression (yellow bracket; 100  $\mu$ m). **b**, 3D rendering (40  $\mu$ m) and **c**, longitudinal cross-section  
560 of LN vessel (20  $\mu$ m) demonstrating absence of  $\beta$ 3-tubulin (dashed circle) where GAP43  
561 expression is present. **d**, **e**, Max projections (50  $\mu$ m) show a  $\beta$ 3-tubulin+GAP43- vessel (**d**) and  
562 a  $\beta$ 3-tubulin-GAP43+ vessel (**e**) indicated with yellow brackets in SPL. **f**, **g**, Max intensity  
563 projection of SPL vessels showing regions of continuous  $\beta$ 3-tubulin, reduced GAP43, and  
564 clustered Coronin-1A expression (dashed outlines; 50  $\mu$ m). **h**, Multiplexed CODEX image of two

565 CD20+ splenic follicles with a CD31+ central artery passing through a PALS region  
566 demonstrating a clustering of CD4+CD45RO+ memory T cells around the artery, in contrast to a  
567 perifollicular distribution of CD8a+ T cells (180  $\mu$ m). Donor ID, tissue, and region are defined to  
568 the right.

569 **Methods**

570 **Donor Acceptance Criteria**

571 SPL and LN were acquired from 14 non-diseased organ donors (Extended Data Table 1)  
572 through the Human BioMolecular Atlas Program (HuBMAP)<sup>3</sup> Lymphatic System Tissue Mapping  
573 Center (TMC) at the University of Florida, via a nationwide organ procurement network. Prior to  
574 organ recovery, written informed consent for research is provided by the donor families. Criteria  
575 for donor acceptance by the HuBMAP Lymphatic System TMC at the University of Florida are  
576 available on the HuBMAP site (<https://www.protocols.io/view/donor-acceptance-criteria-for-tmc-florida-zurich-h-bipykdpw>) and as follows: donors less than 7 days on a ventilator, tissue  
577 received within 24 hours of recovery, and donor body mass index (BMI) between the 5<sup>th</sup> and 95<sup>th</sup>  
578 percentile as defined by the United States Centers for Disease Control and Prevention (CDC).  
579 Contraindications for acceptance include: more than four blood transfusions, autoimmune  
580 disease, chromosomal abnormalities, positive culture for bacterial or viral meningitis, or  
581 methicillin-resistant *Staphylococcus aureus* (MRSA), sepsis, observable infarction, rupture, SLP  
582 or LN deflation or gross abnormality, immune deficiency disease, cancer, infection including  
583 severe acute respiratory syndrome-coronavirus-2 (SARS-CoV-2), and splenomegaly.  
584

585

586 **SPL and LN Case Processing and Quality Control (QC)**

587 Human SPL and mesenteric LN were processed within 16 hours of cross clamp. Residual fat or  
588 connective tissues were removed from each LN and size (mm) recorded. LN > 1 cm<sup>2</sup> were  
589 bisected to 1 cm<sup>2</sup>. LN < 1 cm<sup>2</sup> were left intact. Intact spleens were photo documented with hilum  
590 to left, inferior end at top. Cross-sectional slabs were cut 1 cm thick, and a 1 cm wide strip was  
591 cut through the center of each slab with the superior pole surface facing up and the hilum  
592 serving as the point of origin. 1 cm<sup>3</sup> blocks were dissected from each strip with all cuts photo  
593 documented for location and orientation. Tissue cassettes were placed in at least 20 volumes of  
594 4% PFA (i.e., 20 mL 4% PFA per 1 mL tissue) for 20-24 hours, transferred to 70% ethanol, and

595 paraffin embedded in an automated tissue processor (Sakura VIP) within 3 days. SPL and LN  
596 were sectioned to 5  $\mu$ m and stained with hematoxylin and eosin (H&E) and evaluated by an  
597 independent pathologist to assess organ normality.

598

599 **Immunohistochemistry**

600 IHC was performed according to HuBMAP Lymphatic System TMC standard operating  
601 procedures (SOPs) as detailed (<https://www.protocols.io/view/dab-staining-of-ffpe-slides-bdiei4be>). Formalin fixed, paraffin embedded (FFPE) human SPL and LN were sectioned to 5  
602  $\mu$ m, mounted on SuperFrost Plus (Fisher Scientific) microscope slides and air dried overnight.  
603 Slides were deparaffinized twice in xylene and 100% ethanol for 5 minutes, peroxidase blocked  
604 with 3% peroxide in methanol for 10 minutes followed by serial ethanol washes (95%, 75% and  
605 50%) each for 5 minutes. Finally, slides were washed in deionized water twice for 5 minutes.  
606 Antigen retrieval involved microwaving at 50% power for 7 minutes in 10 mM sodium citrate  
607 buffer pH 6.0 followed by an 18 minutes incubation in the hot citrate. Slides were then  
608 rehydrated with 50mM Tris buffered saline pH 7.6 with 0.1% Tween (TBST) for 5 minutes in a  
609 humidified chamber. Diaminobenzidine (DAB) staining was performed using VECTASTAIN Elite  
610 ABC Kit (peroxidase-HRP) kit (Vector Labs) and IMPACT DAB (peroxidase substrate). Avidin  
611 and biotin were sequentially blocked using Avidin/Biotin Blocking Kit (Vector Labs) for 20  
612 minutes, followed by TBST rinse and incubation in 2% normal serum block (in TBST) for 1 hour.  
613 Primary antibodies were diluted in Antibody Diluent Reagent Solution (Life Technologies;  
614 Supplemental Table 1), applied to the slide, covered with a plastic coverslip and incubated  
615 overnight at 4°C in humidified chamber. Slides were incubated with diluted biotinylated  
616 secondary antibodies (5  $\mu$ l antibody, 15  $\mu$ l serum and 1 mL TBST) for 30 minutes at room  
617 temperature followed by addition of ABC Reagent for 30 minutes. Diluted DAB reagent was then  
618 added, development observed microscopically and reaction stopped in tap water. Slides were  
619 added, development observed microscopically and reaction stopped in tap water. Slides were

620 then counterstained with hematoxylin followed by alcohol and xylene dehydration and cover-  
621 slipped.

622

### 623 **CODEX Antibody Conjugation and Validation**

624 Commercially available oligonucleotide conjugated antibodies were purchased from Akoya  
625 Biosciences and used at a standard dilution of 1/200 (Supplemental Table 1). Akoya CODEX  
626 antibody validation consists of comparing its oligo-conjugated antibodies with dye-conjugated  
627 antibodies to assure equivalent staining pattern, antibody titration for optimal signal, and single  
628 and multiplex staining for consistent staining patterns (<https://www.akoyabio.com/wp->  
629 [content/uploads/2022/01/Phenocycler\\_Technical-Note\\_Validation-of-Commercial\\_DN-00140.pdf](https://www.akoyabio.com/wp-content/uploads/2022/01/Phenocycler_Technical-Note_Validation-of-Commercial_DN-00140.pdf)). For custom conjugation, purified, carrier-free, antibodies are purchased from  
630 reputable vendors, providing validation data including IHC-Paraffin and western blots. All  
631 antibodies, including commercially available CODEX antibodies are validated by IHC in our lab  
632 using the tissue of interest. Barcodes are assigned to antibodies based on the abundance and  
633 intensity of the protein expression. Less abundant antigens are assigned to fluorescence  
634 channels having lower natural autofluorescence, namely Cy5 and AF750. Conversely,  
635 antibodies for highly expressed antigens can be assigned to ATTO550 where tissue  
636 autofluorescence is higher. Conjugations were performed with commercially available CODEX  
637 Conjugation Kits (Akoya Biosciences) according the manufacturer's recommendation with the  
638 following modifications. Briefly, for each antibody, a 50 kDa molecular weight cut-off (MWCO)  
639 filter (Amicon Ultra) was washed with Filter Blocking Solution, centrifuged at 12,000 xg for 2  
640 minutes and emptied of all liquid. To concentrate the antibody, 50 µg of protein, as determined  
641 by Nanodrop absorbance, was diluted in 100 µl PBS, added to the filter and centrifuged at  
642 12,000 g for 8 minutes. To initiate the disulfide reduction reaction, Antibody Reduction Master  
643 Mix was added to the filter, vortexed for 2-3 seconds, incubated at room temperature for no

645 more than 25 minutes followed by buffer exchange. A unique barcode was prepared for each  
646 antibody (Supplemental Table 1) by reconstituting in 10  $\mu$ l distilled water, adding 210  $\mu$ l of the  
647 Conjugation Solution with incubation at room temperature for 2 hours. 5-10  $\mu$ l of antibody  
648 solution was reserved for protein electrophoresis, and the filter washed three times with  
649 Purification Solution. Newly conjugated antibodies were collected by centrifugation. Custom  
650 conjugated antibodies were titrated (1/200, 1/100, 1/50) and validated by comparing the staining  
651 patterns of each conjugated antibody alone in CODEX against IHC DAB staining before being  
652 included in multiplex experiments. Newly conjugated antibodies were also stained alongside  
653 positive and negative controls in the CODEX platform as described  
654 (<https://www.protocols.io/view/hubmap-tmc-uf-validation-of-custom-conjugated-anti-bkpzkvp6>).  
655 All antibodies, including commercially available CODEX antibodies are validated by IHC in our  
656 lab using the tissue of interest. Barcodes are assigned to antibodies based on the abundance  
657 and intensity of the protein expression. Less abundant antigens are assigned to fluorescence  
658 channels having lower natural autofluorescence, namely Cy5 and AF750. Conversely,  
659 antibodies for highly expressed antigens can be assigned to ATTO550 where tissue  
660 autofluorescence is higher.

661

## 662 **CODEX Staining**

663 Oligonucleotide barcoded antibody staining of tissue sections mounted on cover slips (n=1  
664 section per tissue region per donor) was performed using a commercially available CODEX  
665 Staining Kit according to the manufacturer's instructions for FFPE tissue (Akoya Biosciences)  
666 and as recorded for HuBMAP Lymphatic System TMC SOPs  
667 (<https://www.protocols.io/view/codex-antibody-staining-protocol-for-ffpe-tissues-bbsdina6>). In  
668 brief, sample coverslips were heated to 55°C, cooled, deparaffinized and rehydrated. Antigen  
669 retrieval was performed using 1X Citrate pH 6.0 in a pressure cooker. Tissue coverslips were

670 washed and equilibrated in CODEX Staining Buffer. Samples were incubated with barcoded  
671 antibodies (diluted as described in Supplemental Table 1) in CODEX blocking buffer for 3 hours  
672 in a humidity chamber at room temperature. After PBS washes, tissue sections were  
673 sequentially fixed with 1.6% paraformaldehyde (PFA), methanol (on ice) and Codex Fixative  
674 Reagent. Stained sample coverslips were stored for up to 2 weeks in CODEX Storage Buffer at  
675 4°C. Barcoded fluorescent reporters corresponding to the barcoded primary antibodies were  
676 added to 96-well plates containing Codex Reporter Stock solution and nuclear stain, in groups  
677 of three (one of each wavelength) for each multiplex cycle (<https://www.protocols.io/view/codex-preparation-of-reporter-96-well-plates-bc2riyd6>).  
678

679

#### 680 **CODEX Image Acquisition**

681 CODEX data were collected using CODEX Instrument Manager (CIM) software version 1.29,  
682 which automates image acquisition. During cycling, the CODEX instrument automatically adds  
683 the reporter solution to the coverslip, acquires fluorescent images, removes the reporters  
684 (DMSO/1X CODEX Buffer wash), and prepares the tissue for the next cycle. Images were  
685 acquired at 20X magnification using a Keyence BZ-X810 microscope with a metal halide light  
686 source, a Plan Apo  $\lambda$ NA 0.75 20X air objective (Nikon), and the following emission filters  
687 (Chroma) and acquisition times: DAPI (358 nm, 10ms), TRITC (550 nm), CY5 (647 nm) and  
688 CY7 (750 nm) Alexa Fluor 750 (500ms), Atto 550 (350ms), and Alexa Fluor 647 (500ms).  
689 Keyence and image settings were multi-color z-stack, excitation light 100%, low photo bleach,  
690 Shadow 0, Highlight 255, gamma 1.0. The camera was set to mono and high resolution.  
691 Images were acquired in 13 cycles with the appropriate number of z-planes for the tissue of  
692 interest at 1.5 pitch: spleen 17 and lymph node 11. To address the consequences of and  
693 changes in autofluorescence during a CODEX experiment, a blank sample was imaged for each  
694 cycle providing a direct assessment of all background signal (autofluorescence). Images were  
695 7x9 (3.77 x 3.58 mm). Raw images were saved in 14bit TIFF (\*.tif) format.

696

697 **CODEX Image Processing**

698 CODEX datasets were processed using the Akoya CODEX Processor 1.7.0.6. Multi-color z  
699 stacks acquired during each cycle were aligned by 3D drift compensation, and the best focal  
700 plane from each z stack was identified and used for quantitation. Specifically, there were four  
701 fluorescent channels with channel 1 (DAPI) used as the reference in cycle 2. Tiling was snaked  
702 by rows with 30% X and Y overlap, and 25 deconvolution iterations using the vectorial model.  
703 The segmentation parameters included: Anisotropic Region Growth, nuclear segmentation  
704 (DAPI), with a radius of 6, concentric circles 0, minimum/maximum cutoffs 0.02/0.99, relative  
705 cutoff 0.01, size cutoff factor 0.01 and inner ring size of 1.0. Advanced parameters included: tile  
706 processing (cycle alignment, background subtraction, deconvolution, extended depth of field),  
707 region processing (shading correction, tile registration, overlap cropping), stitching, full stitching,  
708 watershed segmentation, t-SNE report generation. Fluidic, temperature, and time dependent  
709 effects could occur between imaging cycles and were addressed with a using 3D phase  
710 correlation function. The calculated offsets were used in the alignment of all cycles as  
711 determined from the comparison of the reference cycle to the nuclear DAPI stain from the  
712 second cycle, for each cycle. Tile registration, from inaccuracies in camera positioning, were  
713 addressed using a Microscopy Image Stitching Tool (MIST) library<sup>79</sup> that finds offsets by utilizing  
714 CUDA FFT phase correlation. Given the potential for variation of background signal across  
715 cycles, the normalized data were derived by subtracting background from each channel using  
716 both the first and last blank cycles. To address potential effects of exposure time, the Akoya  
717 software provides a ratio of signal exposure time to blank exposure time. For visualization  
718 purposes, some images had brightness subject to adjustment.

719

720 **Cell-Based and Neighborhood Analyses**

721 We utilized the Akoya CODEX Multiplex Analysis Viewer (CODEX MAV; version 1.5.0.8 9)  
722 plugin in ImageJ (version1.53f51) for image analysis. The MAV software allows for image  
723 navigation, cell segmentation and biomarker quantification with clustering of cellular phenotypes  
724 accomplished by an X-shift clustering algorithm<sup>42</sup> based on nearest neighbor density estimation.  
725 The cell types/clusters were manually annotated based on phenotype marker expression and  
726 displayed as an intuitive heatmap. Cell counts from each cluster from 5 LN and 5 SPL were then  
727 displayed as the percent of the total cell population. Voronoi analyses implemented as part of  
728 CODEX MAV were employed to illustrate separate B cell populations derived from marker-  
729 based annotation coupled with cellular localization. Neighborhood analyses for total data sets as  
730 well gated data subsets were displayed using dimensionality reduction and t-SNE visualization  
731 via the CODEX MAV software plugin.

732 Pixel-based pair-wise colocalization analyses were performed using the Coloc2 plugin  
733 (ImageJ/Fiji)<sup>80</sup> to obtain Pearson's correlation coefficients for respective protein marker pairings.  
734 Pearson correlation analysis, with R values near 1 indicating complete colocalization and R  
735 values near 0 indicating no colocalization of pixels above threshold intensity.

736

### 737 **Tissue Clearing**

738 A CLARITY<sup>81</sup> based protocol was used to clear tissues. All incubation and wash steps were  
739 performed with gentle rocking. Samples (< 1 cm<sup>3</sup>) were fixed in 40 mL of 4% PFA (Electron  
740 Microscopy Sciences) for 24 hours at 4°C, incubated for five days at 4°C in 40 mL of hydrogel  
741 monomer solution [4% acrylamide (Bio-Rad), 0.05% bis-acrylamide (Bio-Rad), 0.25% VA-044  
742 Initiator (Wako Specialty Chemicals), 4% PFA, in PBS], then polymerized for 5 hours in 50 mL  
743 PBS at 37°C. Hydrogel embedded tissues were then cleared of lipids by incubating in 50 mL of  
744 clearing solution (Logos Bio) at 60°C, replacing clearing solution weekly until optically  
745 transparent. Cleared samples were washed in PBS with 0.1% Triton X-100 (PBST) for 48 hours  
746 at 37°C, replacing PBST wash buffer every 12 hours. The HuBMAP Lymphatic System TMC

747 receives 1 cm<sup>3</sup> pieces of SPL and LNs of varying sizes, ranging from 1 mm<sup>3</sup> to 0.5 cm<sup>3</sup>.  
748 Samples are further portioned to test multiple immunolabeling combinations, generally we  
749 image 0.25 cm<sup>3</sup> pieces of SPL, which is ~1% of the total spleen volume; whereas we image  
750 ~50% of each intact LN.

751

### 752 **Immunolabeling and LSFM 3D Imaging/Analysis**

753 All incubation and wash steps were performed with gentle rocking. Cleared samples were  
754 immunolabeled by first incubating in 10 mL RTU Blocker and Diluent (Vector Laboratories) for  
755 48 hours at room temperature. Primary antibodies (Supplemental Table 1) were diluted (1/200)  
756 in RTU Blocker and Diluent for 3 mL total volume added to samples, then incubated for five  
757 days at 37°C, then two days at 4°C. Samples were washed in 50 mL PBST at room temperature  
758 for five days, exchanging PBST wash buffer each day. Secondary antibodies (Supplemental  
759 Table 1) were diluted (1/200) in 5 mL RTU Blocker and Diluent, and samples were protected  
760 from light and incubated for five days at 37°C, then two days at 4°C. Samples were washed in  
761 50 mL PBST at room temperature for five days, exchanging PBST wash buffer daily.

762 Immunolabeled samples were incubated in 20%, 40%, then 63% 2,2'-thiodiethanol  
763 (Sigma Aldrich) diluted with PBS at room temperature for two hours each to attain a refractive  
764 index of n = 1.45. Samples were then adhered to a glass capillary using cyanoacrylate to mount  
765 into the light sheet imaging chamber. Images were obtained with a Zeiss Z.1 Lightsheet  
766 microscope using a 20x objective. Images were processed with Arivis Vision4D software  
767 (v.3.0.1) and are presented as single optical sections, max intensity projections, and 3D  
768 renderings. Quantification of 3D volumes was conducted with Arivis Vision4D in the following  
769 manner: image volumes were cropped to isolate structural features of interest, then a  
770 supervised intensity-based segmentation was performed using the ‘magic-wand’ feature to  
771 isolate channel specific objects, from which volumetric output was derived.

772

773 **Data availability statement**

774 The data generated and/or analyzed during the current study are publicly available in the  
775 HuBMAP repository. Specifically, the complete CODEX datasets (unprocessed, processed data,  
776 along with blank and DAPI channels) with all markers are available on the HuBMAP data portal  
777 ([https://portal.hubmapconsortium.org/search?entity\\_type\[0\]=Dataset](https://portal.hubmapconsortium.org/search?entity_type[0]=Dataset)).

778 **Methods References**

779 79 Chalfoun, J. *et al.* MIST: Accurate and Scalable Microscopy Image Stitching Tool with  
780 Stage Modeling and Error Minimization. *Scientific Reports* **7**, 1-10 (2017).  
781 <https://doi.org:doi:10.1038/s41598-017-04567-y>

782 80 Rajani, S., Gell, C., Abakir, A. & Markus, R. Computational Analysis of DNA  
783 Modifications in Confocal Images. *Methods in Molecular Biology* **2198**, 227-254 (2021).  
784 [https://doi.org:10.1007/978-1-0716-0876-0\\_19](https://doi.org:10.1007/978-1-0716-0876-0_19)

785 81 Chung, K. & Deisseroth, K. CLARITY for mapping the nervous system. *Nature Methods*  
786 **10**, 508-513 (2013). <https://doi.org:10.1038/nmeth.2481>

787 **Acknowledgements**

788 We thank the families of the organ donors for the gift of tissues. This work was supported by a  
789 grant from the NIH NIAID (U54AI142766) to MAA, HSN, TMB, and CHW as well as  
790 (P01AI042288) to MAA, The Leona M. and Harry B. Helmsley Charitable Trust (G-2004-03813)  
791 to MAA, and JDRF (5-SRA-2018-557-Q-R) to MAA.

792

793 **Author Contributions**

794 SC, MJ, JAN, MAB, HH, and CHW performed the experiments and/or analyzed the data. SC,  
795 MJ, MAB, JPA, NR, MMS, MY, IK contributed to donor organ acquisition and processing. SC,  
796 HSN, CHW, and MAA designed the research. HSN, KO, TMB, CHW, and MAA supervised the  
797 research. SC, HSN, and CHW integrated the data and interpreted the results. SC, HSN, CHW,  
798 ALP, and MAA wrote the manuscript. All authors discussed the results and edited the  
799 manuscript.

800

801 **Competing Interest Declaration**

802 The authors declare no competing interests.

803

804 **Additional Information**

805 Supplementary information is available for this paper.

806 Correspondence and requests for materials should be addressed to Mark A. Atkinson, PhD.

807 **Extended Data Figure and Table Legends**

808 **Extended Data Table 1. Donor demographics, clinical information, and tissue sample**  
809 **identification numbers for SPL and LN examined by IHC, CODEX, and LSFM.**

810

811 **Extended Data Figure 1. Immunohistochemical assessment of immune, nervous,**  
812 **endothelial, and stromal markers in human LN and SPL.** CD3 $\epsilon$ , CD4, CD8 $\alpha$ , CD20, CD21,  
813 CD15, Coronin-1A, CD31, CD34, Vimentin, CD107a, CD163, PGP9.5,  $\beta$ 3-tubulin, GAP43,  
814 ChAT, TH, LYVE1, PDPN and PROX1 were visualized by chromogen-based IHC in human LN  
815 (left) and SPL (right) to confirm anticipated staining pattern and determine appropriate antibody  
816 dilutions. DAB (brown) indicates a positive signal. Red arrows identify fine neural processes of  
817 PGP9.5 within insets of LN and SPL (100  $\mu$ m).

818

819 **Extended Data Figure 2. Immune cell organization within human LN and SPL.** CODEX  
820 images of **a,b,c**, LN and **d,e,f**, SPL wide-field (top left, 560  $\mu$ m) along with high resolution  
821 images (30  $\mu$ m) depicting immune cell distribution throughout tissue parenchyma. **a, d**, CD20  
822 highlights B cells in follicles supported by CD21+, CD35+ FDC meshwork. **b,e**, CD20+ B cells  
823 are organized in follicles with admixed CD4+ and CD8+ T cells in the interfollicular space. The  
824 periphery of select follicles demonstrates enrichment for CD4+CD45RO+ memory helper T  
825 cells, which may represent T follicular helper cells. In the SPL, CD3-CD8 $\alpha$ + cells defining the  
826 LCs line the venous sinusoids. **c**, CD15+ neutrophils and CD68+ macrophages are sparsely  
827 distributed throughout LN cortex. **f**, In SPL, CD15+ neutrophils are highly abundant both  
828 circulating in sinuses and concentrated around follicles throughout the red pulp while CD68+  
829 macrophages are found primarily in the red pulp cords. Donor ID, tissue, and region are defined  
830 to the right of each row.

831

832 **Extended Data Figure 3. Representative organization of LEC, BEC, and stromal cells in**  
833 **human LN.** Representative CODEX images from five LNs of four independent donors (120  $\mu$ m).  
834 **a**, LYVE1 highlights sinus lymphatics with PROX1 labeling LEC nuclei. LYVE1+ sinusoids,  
835 CD4+ T cells admixed with CD8a+ T cells in the perisinusoidal space and Vimentin staining the  
836 background stroma (*middle*). CD31 and CD34 identify BECs with SMA accentuating arterioles  
837 (*left*). CD163+ macrophages in the perisinusoidal space, and CD15+ neutrophils can be seen  
838 emerging from the LYVE1+ sinus (*right*). **b-d**, Additional regions from three donor LNs show the  
839 distribution of LYVE1 and PDPN expression within perivascular lymphatic sinuses as identified  
840 by CD31, CD34, and SMA. **e-g**, Three Additional LN regions from two donors with LYVE1+  
841 sinusoids, CD4+ T cells admixed with CD8a+ T cells in the perisinusoidal space and Vimentin  
842 staining the background stroma. **h-j**, Additional LN regions from two donors showing a similar  
843 pattern as described in e-g with CD8+CD107a+ T cells and CD163+ macrophages in the  
844 perisinusoidal space. Donor ID, tissue, and region are defined to the right of each panel.  
845

846 **Extended Data Figure 4. Representative organization of LEC, BEC, and stromal cells in**  
847 **human SPL.** Representative CODEX images of five SPL regions from three independent  
848 donors (120  $\mu$ m). **a-c**, LYVE1 highlights splenic lymphatics while SMA and PDPN highlight a  
849 trabecula. A CD31+SMA- venules are present and PDPN co-expression is also seen in other  
850 smaller SMA+ splenic arterioles. **d-f**, LYVE1+CD8a+ LCs are present with Vimentin highlighting  
851 background stroma. Note the distribution of CD4+ T cells around a PALS (unstained, dashed  
852 oval, d), early follicle (e), and within the cords of Billroth (f) versus CD8+ T cells. **g-i**, LYVE1  
853 again highlights LCs with CD8a coexpression, and the cords of Billroth show a regular  
854 distribution of CD8a+CD107a+ T cells and CD163+ macrophages. Donor IDs and regions are  
855 defined to the right of each panel.  
856

857 **Extended Data Figure 5. Highly multiplexed CODEX images of immune, stromal, and**  
858 **myeloid cells in human LN and SPL along with marker colocalization analysis.** **a.** The LN  
859 shows CD20+ B cells organized into follicles with perifollicular CD4+CD3e+CD45RO+ memory  
860 T cells (likely T follicular helper) that distribute to nearby CD31+ vasculature. CD3+CD8+ T cells  
861 show a somewhat patchy distribution closer to the vasculature and sparing the follicles. HLA-  
862 DR+ antigen presenting cells are scattered adjacent to the follicle and vasculature with signal  
863 from the CD35+/CD21+ FDCs appearing in the follicles. **b.** The SPL shows a CD31+ arteriole  
864 with a white-pulp periarteriolar follicle containing CD20+ B cells and CD21+/CD35+ FDCs. The  
865 follicle also contains HLA-DR+ antigen presenting cells, likely dendritic cells. CD8 finely  
866 highlights the LCs near which lie CD31+ venules. CD4+CD45RO+ memory T helper cells  
867 appear distributed throughout the follicle, rather than the follicle periphery as seen in the LN (a)  
868 which implies a difference in follicle age between the two sections. CD3e+CD4-CD8- NK cells  
869 are better appreciated in this SPL section than in the LN (a). **c.** LYVE1 highlights LN sinusoidal  
870 LECs with focal PDPN expression. PDPN is also identified in the CD21+ follicle. CD31+CD34+  
871 venules and CD31+CD34+SMA+ arterioles are noted. CD68 and CD163 highlight macrophages  
872 mostly within the lymphatic sinus and a few CD107a+ interfollicular cytotoxic lymphocytes are  
873 noted. Vimentin demonstrates the background stromal architecture (120  $\mu$ m). **d.** SPL sinuses  
874 are demonstrated by CD31, CD34 and LYVE1 with PDPN highlighting a component of an SMA+  
875 arteriole. CD68+CD163+ macrophages and CD107a+ cytotoxic lymphocytes are distributed in  
876 the cords of Billroth with a small periarteriolar follicle identified by CD21+ follicular dendritic  
877 meshwork. Donor ID and tissue region are defined to the right of each row. **e,f,** Pearson's R  
878 values derived from pair-wise pixel-based colocalization analyses (Coloc2, ImageJ) for multiple  
879 protein pairs (N=15 SPL and N=14 LN samples, mean and SD shown in red).  
880

881 **Extended Data Figure 6. Cell clustering, segmentation, and t-SNE visualization of high-**  
882 **parameter imaging data from human LN.** Parallel analysis of CODEX images from LN (N=4)

883 with **a-d**, donor ID and tissue region defined to the right of each panel. Each panel displays  
884 supervised X-shift clustering with identical coloring for each cluster used throughout (*upper left*),  
885 heat maps illustrating the protein markers that define each cluster and respective cell counts  
886 (*upper middle*), as well as wide-angle and zoomed-in Voronoi diagrams pseudo-colored by  
887 cluster assignment (*upper right*). Corresponding t-SNE plots (*lower*) demonstrate global  
888 clustering as well as t-SNEs gated for T cells, B cells, neutrophils/macrophages, and endothelial  
889 cells. All analyses were performed with the Akoya CODEXMaV plugin to NIH Fiji using native  
890 algorithm parameters.

891

892 **Extended Data Figure 7. Cell clustering, segmentation, and t-SNE visualization of high-**  
893 **parameter imaging data from human SPL.** Parallel analysis of CODEX images from SPL  
894 (N=4) with **a-d**, donor ID and tissue region defined to the right of each panel. Each panel  
895 displays supervised X-shift clustering with identical coloring for each cluster used throughout  
896 (*upper left*), heat maps illustrating the protein markers that define each cluster and respective  
897 cell counts (*upper middle*), as well as wide-angle and zoomed-in Voronoi diagrams pseudo-  
898 colored by cluster assignment (*upper right*). Corresponding t-SNE plots (*lower*) demonstrate  
899 global clustering as well as t-SNEs gated for T cells, B cells, neutrophils/macrophages/littoral  
900 cells, and endothelial cells. All analyses were performed with the Akoya CODEXMaV plugin to  
901 NIH Fiji using native algorithm parameters.

902

903 **Extended Data Figure 8. CD31 in SPL highlight endothelium and associated elements**  
904 **entering the *tunica media*.** **a**, Photographs of human LN prior to (left) and after (right) tissue  
905 clearing using the CLARITY protocol. **b**, Max intensity projection (*left*, 100  $\mu$ m) and single cross-  
906 section (*right*, 50  $\mu$ m) of a CD31+ blood vessel in spleen. **c**, Max intensity projection of CD31+  
907 splenic blood vessel with DAPI nuclear stain (20  $\mu$ m). **d**, Cartoon depicting neuronal elements  
908 (tyrosine hydroxylase [TH], ChAT,  $\beta$ 3-tubulin, and PGP9.5) observed upon the arterial

909 architecture localized to the *tunica externa*, while GAP43 is limited within either the *tunica media*  
910 or *tunica intima* (created with BioRender.com; adapted from<sup>56</sup>). **e**, Max intensity projection (*left*,  
911 *center left*, and *center right*, 50  $\mu\text{m}$ ) and cross section (*far right*, 20  $\mu\text{m}$ ) of autofluorescence in  
912 splenic blood vessels ensheathed by neuronal processes expressing TH demonstrating  
913 localization to the *tunica externa*.

914

915 **Extended Data Figure 9. LN Lymphatic vessel and nerve fiber networks.** **a**, LSFM max  
916 intensity projections of the extensive  $\beta$ 3-tubulin+GAP43+ vessel network (10  $\mu\text{m}$ ). **b**, LSFM 3D  
917 renderings of LN stained for  $\beta$ 3-tubulin and GAP43 (*upper*),  $\beta$ 3-tubulin+ vessel with a single  
918 GAP43+ nerve fiber overlay (*three lower left panels*, 150  $\mu\text{m}$ ), as well as a max intensity  
919 projection (75  $\mu\text{m}$ ) with inset image of cross-section (50  $\mu\text{m}$ ) demonstrating a GAP43+ filament  
920 nested within the  $\beta$ 3-tubulin+ vessel (*lower right*).

921

922 **Extended Data Figure 10. 3D quantification of neuronal markers in vascular segments**  
923 **associated with differential expression and lymphocyte accumulation in human LN and**  
924 **SPL.** **a**, 3D rendering of blood vessel segments from human LN demonstrating differential  
925 expression of GAP43 and  $\beta$ 3-tubulin, with the control segment demonstrating GAP43 volume at  
926 55% of total  $\beta$ 3-tubulin volume, whereas a target segment demonstrates reduced GAP43  
927 volume at 34% of total  $\beta$ 3-tubulin volume. **b**, 3D rendering of blood vessel segment in LN found  
928 to have no appreciable  $\beta$ 3-tubulin among a GAP43+ vessel. **c**, 3D rendering of blood vessel  
929 segments from human SPL demonstrating differential expression of GAP43 and  $\beta$ 3-tubulin, with  
930 the control segments A and C illustrating GAP43 volume at 41% of total  $\beta$ 3-tubulin volume in  
931 regions without appreciable Coronin-1A<sup>+</sup> cells, whereas target segment B demonstrates GAP43  
932 volume at 3% of total  $\beta$ 3-tubulin volume in a region displaying significant Coronin-1A<sup>+</sup>  
933 lymphocyte accumulation. **d**, An additional vascular segment showing reduced GAP43<sup>+</sup> volume

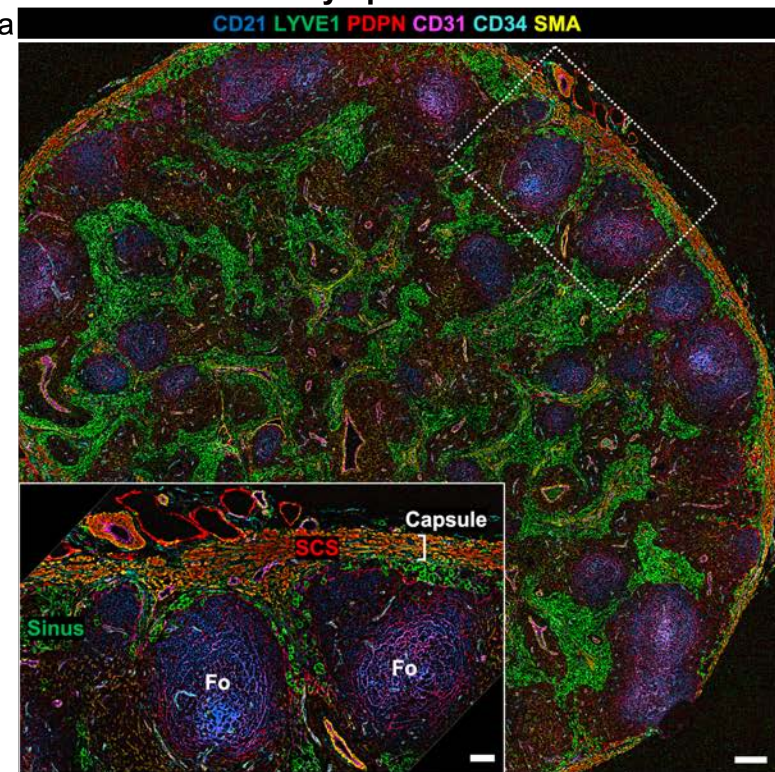
934 at 4% of  $\beta$ 3-tubulin volume in a region containing Coronin-1A<sup>+</sup> cell accumulation. Donor IDs are  
935 defined to the right of each organ dataset. \* Indicates coordination with primary figures.

936

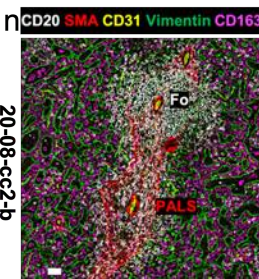
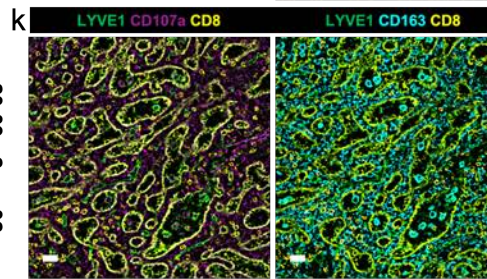
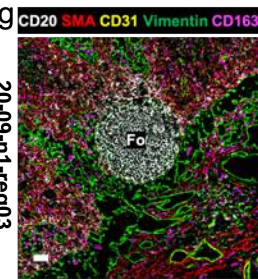
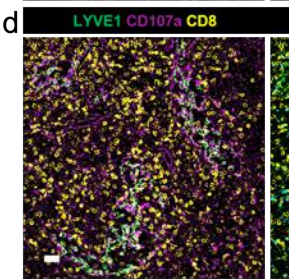
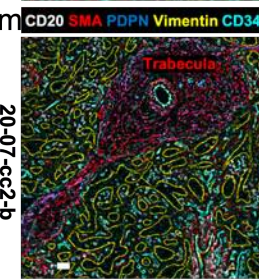
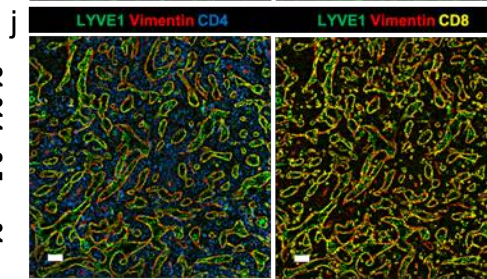
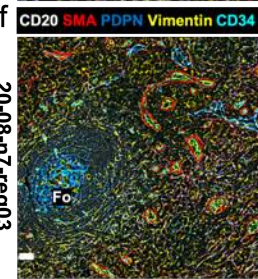
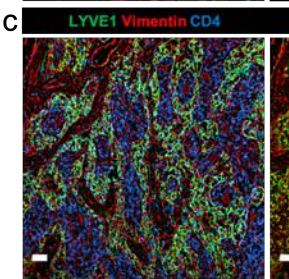
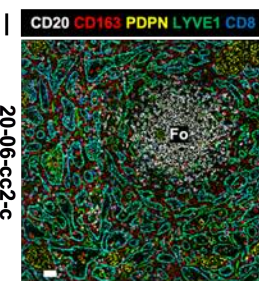
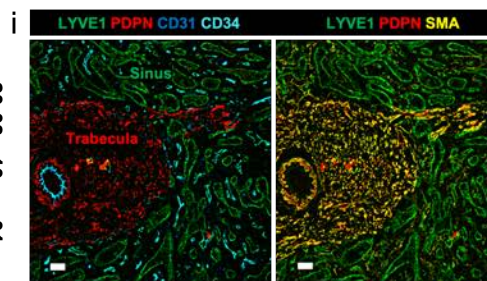
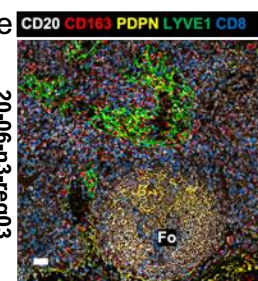
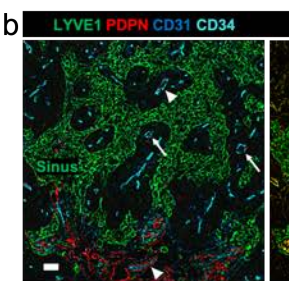
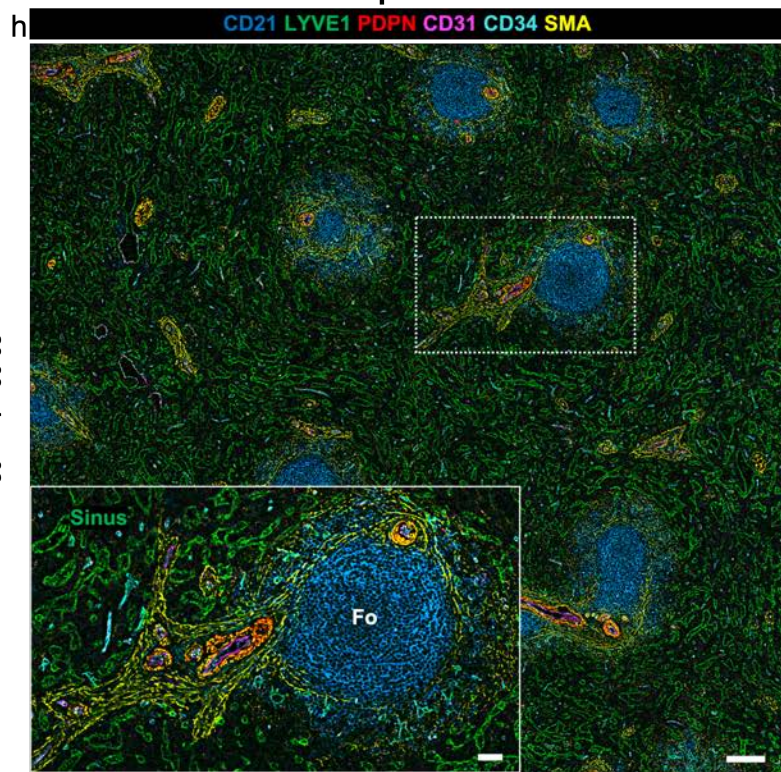
937 **Extended Data Figure 11. CODEX data demonstrating lymphocyte (CD20+ B cells and**  
938 **CD45RO+ memory T cells) accumulation around vascular segments in human SPL.**

939 Representative CODEX images of CD31+PDPN+ vascular segments within six CD20+ follicles  
940 in a single donor SPL (750  $\mu$ m). Numbered insets (90  $\mu$ m) correspond to follicles identified in  
941 top left image. Similar findings were observed across donors with bottom row showing follicles  
942 from two more donor SPLs (90  $\mu$ m). Note the distribution of CD45RO+ memory T cells with  
943 regard to the vessels and follicle. Donor IDs and tissue CCF region are defined within each  
944 representative image.

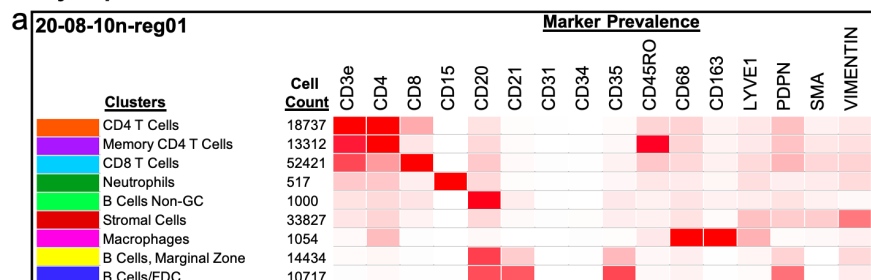
### Lymph Node



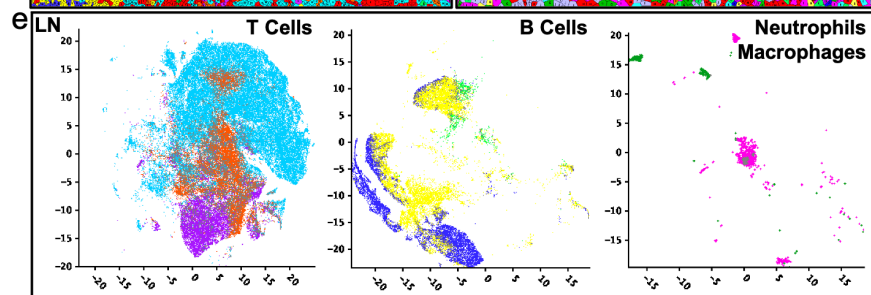
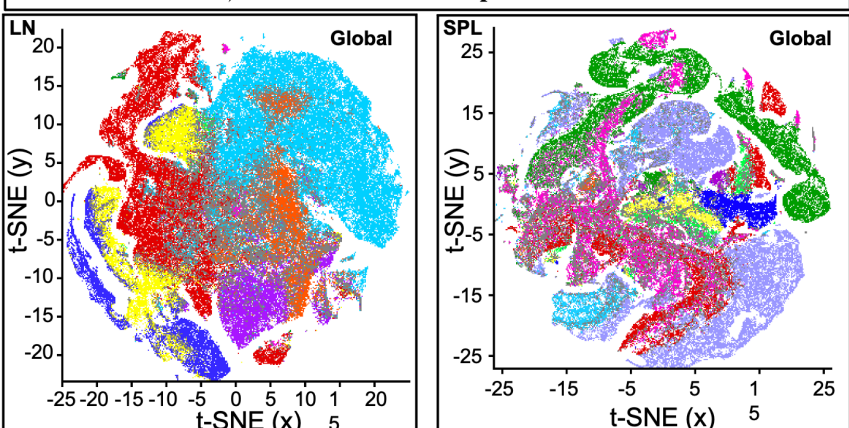
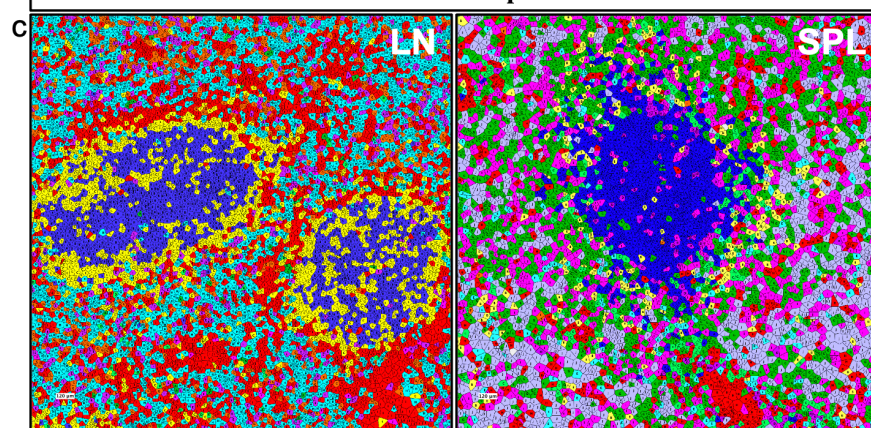
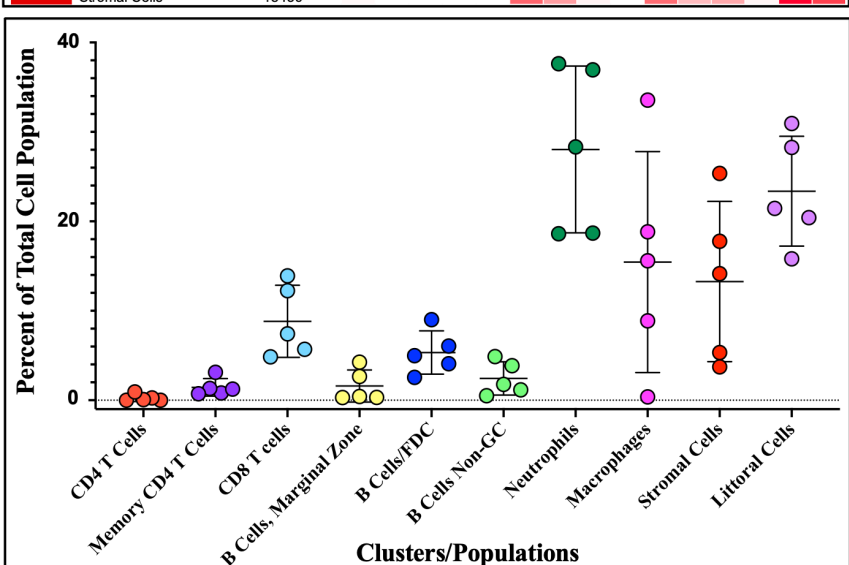
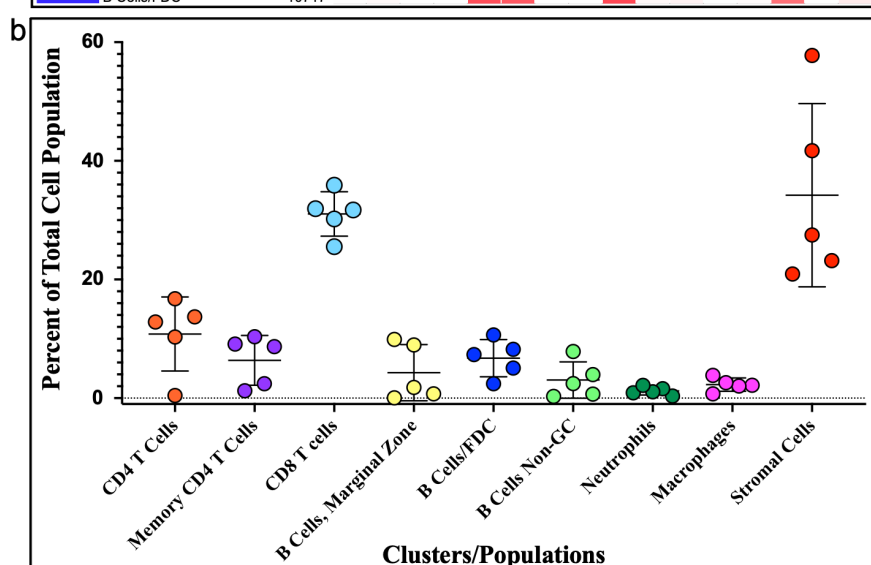
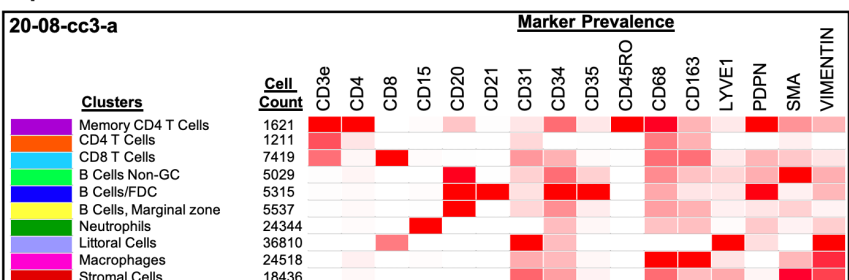
### Spleen



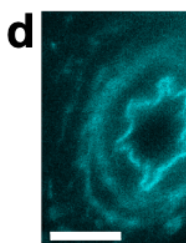
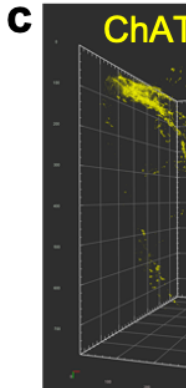
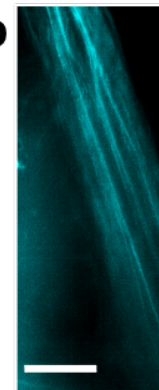
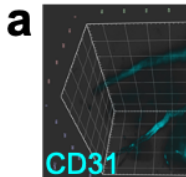
# Lymph Node



# Spleen

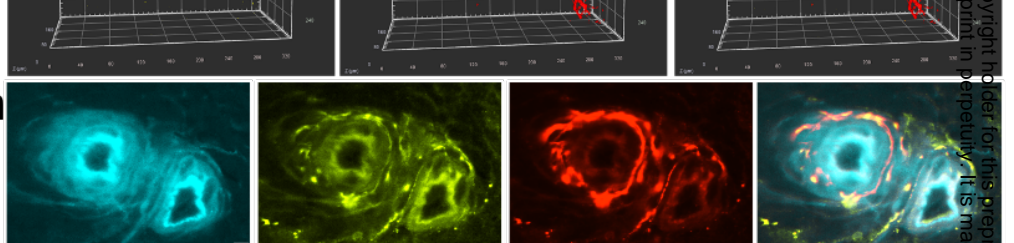
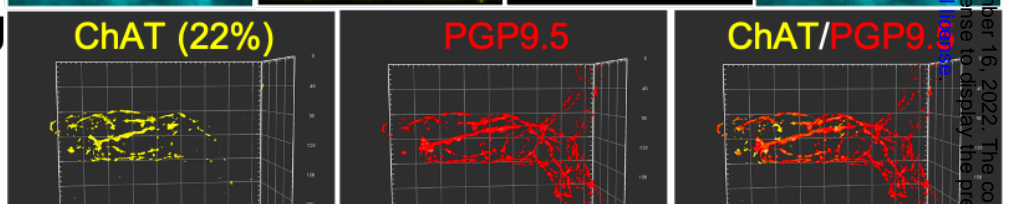
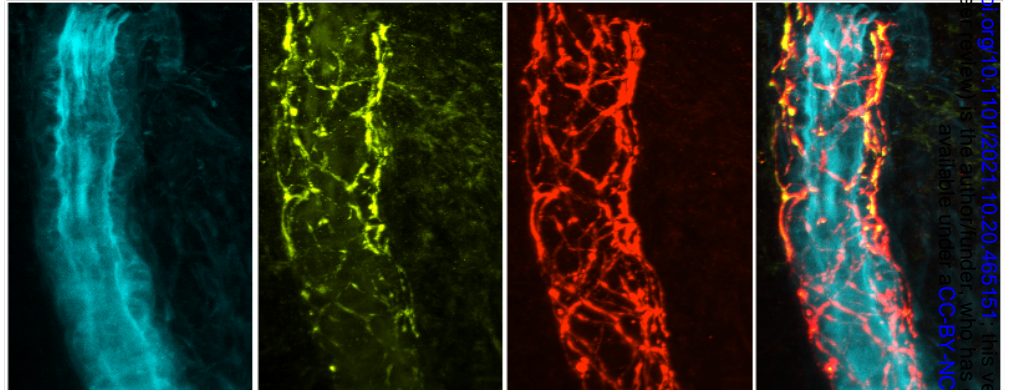
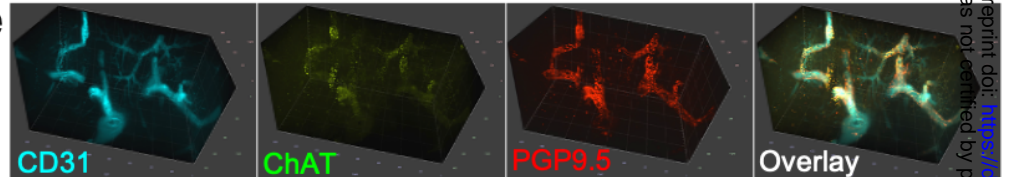


## Lymph Node

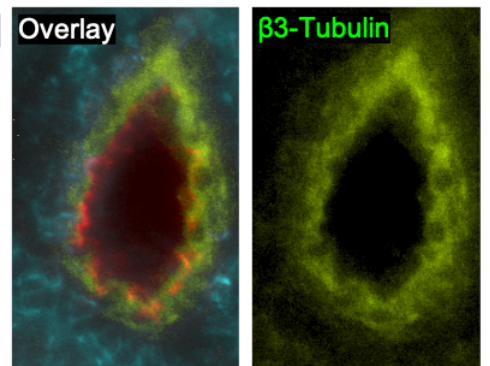
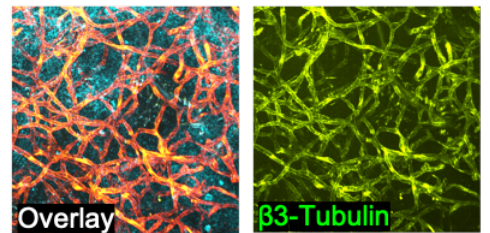
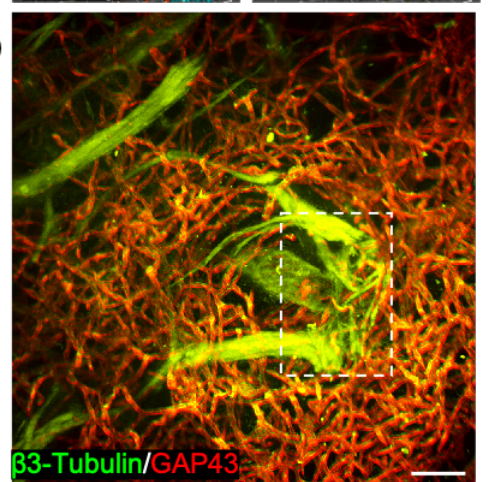
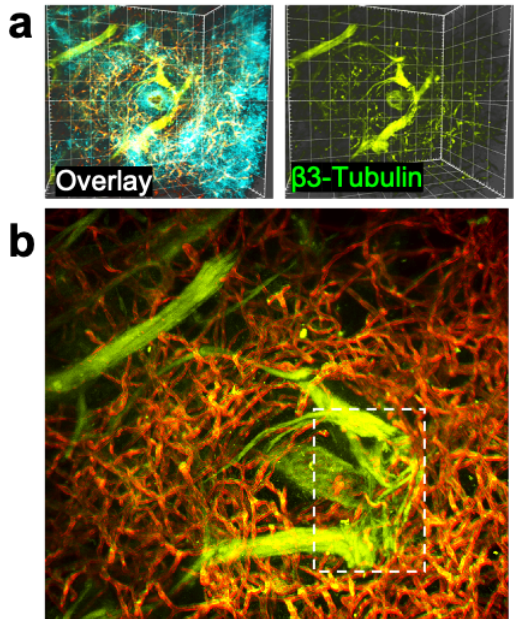


## 20-05-n2-reg01

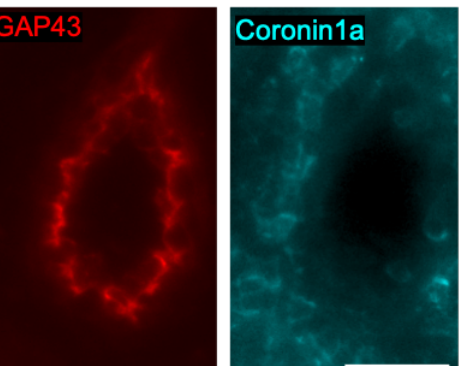
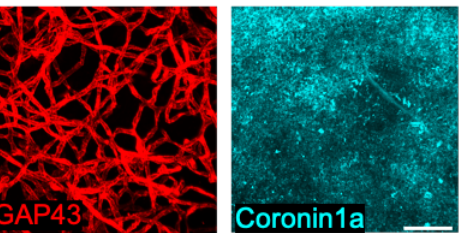
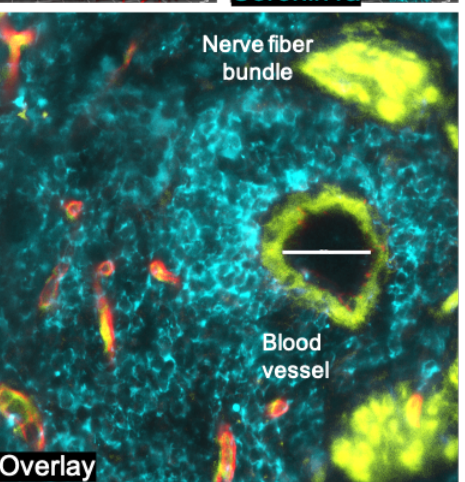
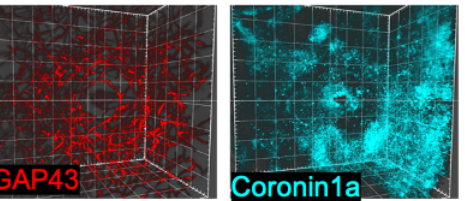
## Spleen



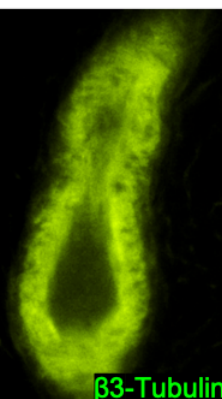
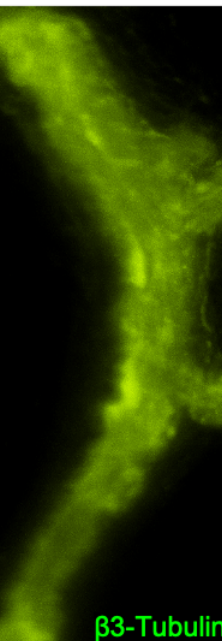
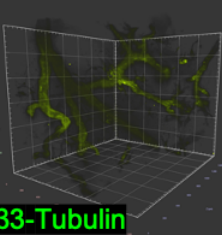
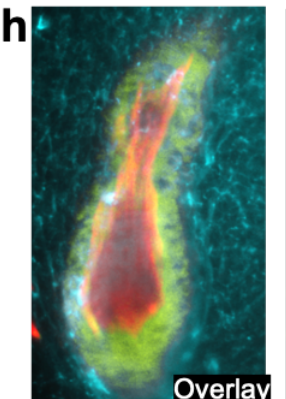
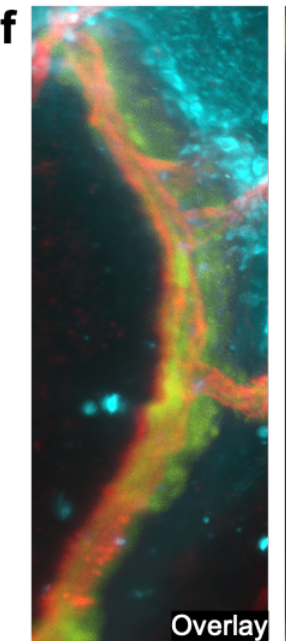
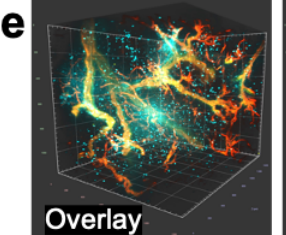
## Lymph Node



## 20-06-n9-reg01



## Spleen



## 19-04-cc2-f

